AEROTHERMAL EFFECTS OF HYPERSONIC SHOCK IMPINGEMENT ON A HIGHLY SWEPT LEADING EDGE

Jonathan Burt
NASA Glenn Research Center
Cleveland, OH

Christopher Marley
NASA Langley Research Center
Hampton, VA

ABSTRACT

A numerical study is conducted to investigate aerothermal implications of oblique shock impingement on a highly swept leading edge in hypersonic flow, with flow conditions and geometry relevant to non-propulsive leading edge heating on hypersonic cruise vehicles. In contrast to propulsive inlet leading edge shock impingement, which has been subject to extensive historical study, bow shock impingement on a highly swept wing leading edge has received comparatively little attention in the literature. Distinguishing characteristics of this type of flow include a potentially dominant surface heating contribution from crossflow-induced viscous dissipation, possible wall velocity slip and temperature jump effects, and various modes of shock layer thermal nonequilibrium that can interact with shock impingement flowfield structures. One overall goal of this work is to assess the impact of bow shock impingement and related nonequilibrium phenomena for wing leading edge design, materials selection and thermal management. Another goal is to improve understanding – and thereby reduce associated design margins – for the physical processes and mechanisms that may influence wing leading edge heating in the presence of an impinging shock. A combination of direct simulation Monte Carlo and Reynolds-averaged Navier-Stokes analysis is used to assess surface and flowfield characteristics for a series of hypersonic shock impingement problems, based on historical ground tests and related flight conditions. Favorable comparisons are performed with experimental data, and various thermal nonequilibrium effects are quantified.

INTRODUCTION

Leading edge shock impingement is known to be a potential source of extremely high local heat loads on hypersonic vehicles. Numerous experimental and computational studies have investigated leading edge heating augmentation in the presence of an impinging shock, and increases in surface heat flux of up to an order of magnitude have been documented [1],[2],[3]. Complex flow structures associated with hypersonic shock impingement on a rounded leading edge have been found to exhibit high sensitivity to both the leading edge geometry and incident shock orientation. Resulting prediction difficulties have led hypersonic vehicle designers to use large heating margins in the vicinity of possible shock impingement regions, with materials selection, thermal protection system thickness, leading edge curvature and cooling strategies potentially dictated by overly conservative heat load estimates. This problem has also led vehicle designers to avoid component geometries and flow conditions that may allow leading edge shock impingement, possibly to the detriment of other design objectives.

BACKGROUND

One prominent historical example of the leading edge shock impingement heating phenomenon is the serious damage experienced by the X-15-2 vehicle during Mach 6.7 operation, when a ramjet test article detached completely as a result of shock-induced structural heating damage to its supporting pylon [4]. Motivated in part by the X-15-2 incident, several experimental studies have been performed to assess surface heating augmentation and to classify flowfield characteristics and structures associated with hypersonic leading edge shock impingement. Edney [1] observed several different types of shock interaction structures, distinguished by the relative orientations of the incident shocks. Subsequent studies have established the general interaction phenomena and expected heating augmentation factors over a variety of conditions. However, very few of these studies have considered flow conditions and geometries relevant to wing leading edge shock impingement, as may occur when distinct laterally propagating shocks are formed near the nose of a vehicle operating at high Mach numbers. Instead, most historical studies have focused on shock impingement in the vicinity of the stagnation region, as when the bow shock hits the cowl leading edge on an airbreathing hypersonic vehicle [2].

In a subset of the larger body of literature on shock-shock interactions, many studies have examined shock impingement on a swept leading edge [5]. Such studies have often focused on flows that are applicable specifically to cowl lip shock interaction problems, for which the incident shock is approximately co-planar with the leading edge. Another class of hypersonic shock impingement flows, which has been observed experimentally [6] but subject to comparatively little detailed historical study, involves three-dimensional bow shock impingement on the highly swept wing leading edge of a hypersonic cruise vehicle. In this case there is no stagnation region due to the presence of crossflow through the shock layer, and important flowfield characteristics can be qualitatively very different.

Despite the fact that bow shock impingement heating augmentation on a swept wing (or tail) leading edge may have important implications for hypersonic vehicle design, surprisingly little is known about this problem. This type of shock interaction, which can be classified as a type of “shock-on-fin” interaction, is characterized by three-dimensional flow structures that should generally be consistent with the standard categorization of Edney [1],[7]. The experimental work of Bushnell in the mid-1960s is one of a few dedicated research efforts on this subject [8],[9]. Results found by Bushnell included the lack of an increase in surface heat flux on an inclined (45° or 60°) cylinder in the vicinity of an impinging oblique shock. A comparison of results from these experiments and the subsequent work of Edney suggests the presence of an Edney Type VI shock-shock interaction [1]. (Note that this interaction type is referred to as “Type I” in Ref. [1] but is widely referenced as Type VI in subsequent publications.)

In contrast to the early findings of Bushnell, significant local heating augmentation was found in subsequent experimental and computational studies of shock-on-fin impingement problems. For example, in another early experimental study, Hiers and Loubsky [7] found a factor of approximately 2.5 increase in leading edge heating for a swept cylindrical leading edge, and reasonably good agreement was observed with results from simplified two-dimensional boundary layer analysis. A subsequent experimental study by Berry and Nowak [10] and a computational study by Singh et al. [11], which both considered flow problems applicable to bow shock impingement heating on a cowl sidewall leading edge, also showed significant local heating augmentation. Berry and Nowak observed strong sensitivity of flowfield structures to the leading edge sweep angle, but the primary emphasis of their study was on forward sweep angles (opposite that of a swept wing-bow shock interaction) for which particularly severe heating is expected. Given historical limitations in the availability of computational resources and high fidelity CFD methods, Singh et al. used comparatively rough modeling assumptions to predict shock interaction heating on a cylindrically blunted and moderately swept (25º) leading edge, and showed relatively good agreement with earlier experimental data of Keyes and Hains [3],[11].

More recently, the Direct Simulation Monte Carlo (DSMC) method was used by Bird [12] to examine three-dimensional bow shock interference on a wire connecting a non-lifting reentry

vehicle with an inflatable aerodynamic decelerator. Flowfield structures in this problem are qualitatively similar to those expected in wing leading edge shock impingement on a hypersonic cruise vehicle, but the high degree of rarefaction – and the correspondingly large global Knudsen number – limit the relevance of this work for hypersonic endo-atmospheric vehicle design.

In reviewing historical studies on three-dimensional "shock-on-fin" interactions, it should be noted that most of these studies focused on geometries or flow conditions of limited relevance to heating prediction for wing leading edge shock impingement [3],[7],[10]-[12]. Important characteristics of these studies which limit applicability to wing leading edge flows include a lack of consideration for large positive sweep angles and a focus on cases involving turbulent or transitional boundary layers. (Laminar shock layers are more likely for hypersonic wing leading edge flows, due to comparatively low gas densities and a stabilizing influence of adverse pressure gradients around the leading edge.) It is also notable that no detailed follow-up work has been performed to fully explain and categorize surface heating characteristics in the early study of Bushnell [8], given that this is one of the very few efforts to investigate hypersonic shock impingement on a highly swept leading edge. Because most related research has focused on cases – relevant to propulsive inlet surfaces – for which large heating augmentation is expected, conditions similar to those of Bushnell appear to have been largely overlooked. Deficiencies in knowledge regarding expected heating characteristics and relevant physical processes for such flow problems may therefore lead to inappropriate assumptions or overly large leading edge heating margins in hypersonic vehicle design.

OVERVIEW OF CURRENT EFFORT

The lack of follow-up studies to that of Bushnell [8] has motivated the current work. To our knowledge, the present effort is the first high-fidelity computational study of hypersonic shock impingement on a highly swept leading edge, based on design considerations for bow shock-wing leading edge interaction on a hypersonic cruise vehicle. This work includes a combination of continuum CFD analysis and calculations employing the direct simulation Monte Carlo (DSMC) method. [13] The NASA FUN3D code [14] is used to provide numerical solutions to the Reynolds-averaged Navier-Stokes (RANS) equations for turbulent flows of calorically perfect gas air. DSMC simulations are performed using the Hypersonic Aerothermodynamics Particle (HAP) code [15], developed at the U.S. Air Force Research Laboratory and NASA, and hybrid simulation capabilities in this code are utilized for efficient simulation of mixed continuum/rarefied flows which present computational challenges for conventional DSMC.

The primary flow problem to be studied in this work is that of Bushnell [8], involving a cylinder which is oriented at high incidence to the freestream direction and positioned downstream of an inclined plate. For reference, a schematic from Bushnell [8] showing the general flowfield characteristics expected for the cylinder-wedge shock interaction is presented as Figure 1. The point labeled A in Figure 1 is the shock intersection point where the oblique shock intersects with the cylinder bow shock. This shock-shock interaction represents an Edney Type VI interaction, with expansion waves and a shear layer (vortex sheet in Figure 1) emanating from the shock intersection point. The flow expands from Region 3 to Region 4 and expansion waves eventually impinge on the cylinder. The expansion waves then reflect off the cylinder and interact with the bow shock.

CFD and DSMC analyses are used here for flows similar to that shown in Figure 1, to characterize flowfield structures across the impingement region, observe various nonequilibrium processes and phenomena (e.g., rotational and vibration nonequilibrium, shock layer rarefaction, wall velocity slip and temperature jump) and compare surface pressure and heat flux with available experimental data. In one component of this work, a series of two-dimensional DSMC calculations (or quasi-two-dimensional calculations, given the presence of crossflow) are used to evaluate shock layer properties independent of the impinging shock. In particular, an approximation of the leading edge geometry from Bushnell is extracted in the edge-normal direction, and two-dimensional DSMC calculations are performed both with and without a crossflow component in the

freestream velocity. A comparison of surface heat flux results between these cases allows heating contributions from crossflow induced viscous dissipation to be determined. Three-dimensional DSMC simulations are also performed for a geometry based on Bushnell's experiment at flight-relevant conditions. Various nonequilibrium phenomena are assessed from results of these simulations through a series of continuum breakdown metrics, and sensitivities to prescribed surface temperature are examined. RANS calculations are performed at higher Reynolds number experimental conditions, in order to evaluate flowfield characteristics and to compare with measured surface heating data.

TWO-DIMENSIONAL NONEQUILIBRIUM ANALYSIS

In this section, DSMC simulations are described for a simplified two-dimensional approximation of laminar hypersonic flow around an inclined cylinder, based on experimental conditions of Bushnell [8]. While some limited comparison with experimental data is performed, the primary focus here is on quantification of nonequilibrium phenomena that may be relevant for surface heating prediction.

PHYSICAL CHARACTERISTICS AND MODELING CHALLENGES

As described above, one distinguishing feature of hypersonic swept leading edge shock impingement is potentially strong spanwise-directed crossflow within the shock layer around the leading edge. Flowfield characteristics associated with the presence of shock layer crossflow may extend to swept wing leading edge flows even in the absence of an impinging shock. In particular, although there is a reduction in surface heat flux due to the decreased shock strength over a swept leading edge, this reduction is countered by an increase in heating associated with viscous dissipation of crossflow bulk kinetic energy across the boundary layer. The crossflow component of freestream velocity remains unaltered through the leading edge shock, and considerable heat is therefore released into the boundary layer as the bulk velocity is reduced to zero (or close to zero) at the surface.

Numerical prediction of hypersonic shock layers with strong crossflow may be further complicated by the resulting increase in velocity and temperature gradients within the boundary layer, where nonequilibrium phenomena – such as wall velocity slip, wall temperature jump, finite rate chemistry, shock layer translational nonequilibrium, and finite rate rotational and vibrational energy exchange – can significantly influence surface heating. Moreover, for large sweep angles, thermal nonequilibrium effects may be strengthened by the relatively weak shock and correspondingly low post-shock density, which in turn lead to increased equilibration time scales. The presence of crossflow may also lead to substantial spanwise boundary layer development and boundary layer transition within a small distance of the leading edge.

Many of these processes can interact in complex ways with flowfield structures resulting from impingement of an incident shock. It follows that, while these processes are typically neglected in leading edge heating analysis, they may require consideration for accurate numerical prediction of shock impingement heating on a highly swept leading edge. The quantitative contributions of several of these phenomena, both individually and in combination, to hypersonic swept leading edge heating are currently either incompletely understood or poorly documented.

SIMULATION SETUP

One component of the current effort is a DSMC-based investigation of thermal nonequilibrium effects, and the corresponding impact on surface heating, in the hypersonic shock layer along a highly swept leading edge. The DSMC method provides a particularly effective means of evaluating thermal nonequilibrium in high-speed flows, and is widely regarded as the most highly developed and most generally applicable numerical scheme for high-fidelity simulation of highly nonequilibrium gas flows. DSMC is a stochastic particle-based technique, in which a large

collection of simulated particles – each representing a very large number of atoms or molecules – move through a simulation domain according to assigned velocities, and periodically participate in binary collisions with other nearby particles. Intermolecular collisions and particle-wall collisions are modeled probabilistically, and particle velocities and internal energy values may vary during impulsive collision events based on theoretical or empirical energy distributions. Unlike conventional deterministic CFD methods, DSMC does not solve a system of governing equations, but instead reproduces (in an approximate manner) the underlying physics of the generalized Boltzmann equation that describes nonequilibrium gas flows. Although it can at times be orders of magnitude more expensive than conventional CFD calculations, DSMC allows for high-fidelity analysis of complex hypersonic flows involving potentially high degrees of translational and internal energy nonequilibrium.

As the basis of swept leading edge shock layer DSMC analysis, the lowest Reynolds number (Re) case of Bushnell [8] involving a 60° inclined cylinder is chosen. This case (with Re_D = 8.9×10^4 based on the cylinder diameter, D) is selected due to an expectation of strongest rarefaction and thermal nonequilibrium effects, and because the comparatively low global Knudsen number (Kn) should allow for reduced computational expense. However, the global Kn of around 2.5×10^{-4}, based on cylinder diameter, is still extremely challenging for DSMC simulation, leading to very high computational expense due to requirements for a large number of particles and a large number of time steps for convergence to steady state. Three-dimensional DSMC simulations have been attempted at test conditions, but were estimated to require over 10^6 CPU hours and unfortunately could not be completed in a timely manner as part of this study. Instead, a set of two-dimensional simulations are performed at test conditions, with complementary three-dimensional simulations at flight-relevant conditions for which freestream total enthalpy is increased while density is reduced.

The two-dimensional simulations, which are conducted to assess shock layer characteristics in the absence of shock impingement, follow from the approximation of an infinitely long cylinder with no spanwise boundary layer development or other spanwise gradients. A simulation, termed the “baseline” simulation, is performed along a slice normal to the cylinder axis, with inflow bulk velocity components both within and normal to the simulation plane. Additional simulations are run with no normal or crossflow inflow velocity component but unchanged in-plane velocity, and at the same Mach number without sweep (i.e., M_∞ = 7.95 with zero normal velocity), to determine the influence of crossflow and sweep on wall heating and on thermal nonequilibrium effects.

As mentioned in the introduction, the HAP DSMC code is employed here. HAP is an adaptive Cartesian grid implementation of DSMC, with a number of unique features intended to reduce computational expense for simulation of low-Kn flows. Some of these features are utilized here, including automated adjustment of time step scaling factors and numerical weight (the number of atoms or molecules represented by each particle) during the transient startup period. Advanced procedures for local dynamic time step interval adjustment are used to ensure the time step (Δt) is uniformly small in comparison to the local mean collision time (MCT, which is related to temporal discretization error due to operator splitting in an explicit numerical solution to the Boltzmann equation) and to preferentially increase particle populations in high-density regions where collision separation requirements for accurate simulation are especially stringent. In particular, the ratio Δt/MCT is set to 0.2 throughout the simulation domain, except within a narrow near-wall region where this ratio is set to 0.05. Nonuniform transient adaptive subcells are also employed to help ensure mean collision separation (MCS) values do not exceed the local mean free path λ, in accordance with standard DSMC guidelines.

As mentioned above, a Re = 8.9×10^4 case of Bushnell [8] with a 60° inclined cylinder is chosen as the basis of DSMC simulations in the present work. More specifically, the 60° separated cylinder geometry from Bushnell is considered here. In this geometry, the cylinder is separated a small distance from the surface of a 12° wedge to minimize the impact of the wedge boundary layer on the shock layer around the cylinder, and an elliptical protruding end-plate aligned with the wedge

surface is fixed to the end of the cylinder. Uniform freestream conditions are assumed, with a total temperature of 738.9 K and a Mach number of 7.95. Simulations are performed for two-species (N_2 and O_2) chemically inert air, which is modeled using the variable hard sphere collision model [13] for which post-collision relative particle velocities are isentropically distributed and transport coefficients vary as power-law functions of translational temperature. The Larsen-Borgnakke model [13] is used for rotational-translational and vibrational-translational energy exchange, with constant collision numbers of 5 and 50, respectively. Note that collision numbers represent a characteristic number of collisions required to equilibrate a given energy mode, and these numbers are used in DSMC as the reciprocal of energy exchange probabilities. Wall boundaries are modeled as isothermal diffusely reflecting walls (i.e., thermal and tangential momentum accommodation coefficient are set to 1) at a temperature of 100°F or 310.9 K as estimated by Bushnell [8]. For the baseline two-dimensional DSMC simulation which includes a crossflow (or out-of-plane) component of inflow velocity, approximately 8×10^7 particles are simulated at steady state, and time-averaged sampling is performed over the last 10^5 time steps out of 2×10^6 total steps. This simulation requires about 30,000 CPU hours on the NASA Pleiades high performance computing system.

SIMULATION RESULTS

Contours of translational temperature from the baseline two-dimensional DSMC simulation (for which inflow velocity includes a component normal to the simulation plane) are presented in Figure 2. The figure shows a rapid temperature rise from the freestream temperature of 54.2 K across the bow shock, with a shock standoff distance slightly smaller than the cylinder radius. A further temperature increase is found around the boundary layer along the cylinder surface, primarily as a result of viscous dissipation associated with crossflow through the shock layer. This crossflow effect is illustrated in Figure 3, where the x-directed (in-plane) and z-directed (out-of-plane or crossflow) bulk velocity components are plotted along the stagnation streamline. (Note that the y-velocity component on this streamline is zero by definition.) The x-directed velocity is shown to decrease sharply across the bow shock, then subsequently decrease almost linearly to zero at the stagnation point. In contrast, the z-directed velocity component – which accounts for most of the total freestream bulk velocity – is unchanged across the shock, and remains at the freestream value outside the boundary layer within a small distance of the wall. Within the boundary layer, the z-velocity slopes sharply downward, approaching a value near (but not equal to) zero at the wall. This drop corresponds to strong viscous dissipation, with the large temperature increase displayed in Figure 2 where bulk kinetic energy is converted to thermal energy.

In Figure 4, translational, rotational and vibrational temperatures are shown along the stagnation streamline (y/D = 0). Results are presented from the baseline simulation (left), as well as an otherwise identical simulation (center) with the crossflow or z-component of inflow bulk velocity set to zero, and a “no sweep” simulation (right) with zero crossflow velocity and the same inflow Mach number as the baseline case. To better indicate trends in and around the boundary layer region, close-up views of this region are shown on the bottom row in Figure 4. Dashed horizontal lines on all plots denote the isothermal wall temperature. Baseline simulation results in Figure 4 show temperatures for all three energy modes that increase rapidly through the boundary layer, overshooting the wall temperature before dropping toward this temperature within a very small distance of the wall. This overshoot is associated with viscous dissipation, and viscous dissipation is in turn dominated by the influence of crossflow velocity.

One clear observation from Figure 4 is that post-shock temperatures are highly dependent on sweep, as is expected from oblique shock relations. The presence of crossflow through the shock layer is found to have a very small but non-negligible positive influence on shock standoff distance, whereas the standoff distance increases considerably due to the influence of sweep. The post-shock translational and rotational temperatures are also nearly independent of crossflow, but are highly sensitive to sweep. As expected, small translational temperature jumps are observed around the bow shock, and only a slight degree of rotational freezing occurs around the shock. Vibrational temperatures for the baseline and “no crossflow” cases are nearly frozen at the

freestream value outside of the boundary layer, due to the very low frequency of vibrational-translational energy exchange associated with shock layer temperatures which are very low in comparison to characteristic vibrational excitation temperatures for the simulated species. In other words, for these cases, collision energies through most of the shock layer are insufficient to promote vibrational excitation beyond the ground vibrational state.

Figure 5 shows contours of the maximum gradient length local Knudsen number ($Kn_{GLL,max}$) for the baseline DSMC simulation. This is a commonly used metric [16],[17],[18] to evaluate continuum breakdown, which occurs when the velocity distribution diverges sufficiently far from the equilibrium or Maxwellian limit to violate underlying assumptions in the governing Navier-Stokes (N-S) equations. In the present work, $Kn_{GLL,max}$ is defined as the maximum of local gradient-based Knudsen numbers

$$Kn_{GLL,q} \equiv \frac{\lambda}{q}|\nabla q| \tag{1}$$

where the scalar quantity q is equal to either number density, pressure, or bulk velocity magnitude, and where λ is the local mean free path. A commonly accepted regime of validity for the N-S equations is $Kn_{GLL,max} < 0.05$, based on computational work showing that this threshold roughly corresponds to 5% error in N-S solutions for hypersonic flows [19]. Values in Figure 5 appear to indicate a lack of continuum breakdown throughout the flowfield. However, the computed $Kn_{GLL,max}$ values – and especially those near the shock – tend to be underpredicted due to a lack of sampling grid refinement in the simulation, with a corresponding underprediction of gradients around narrow flowfield structures. It should be emphasized that the underprediction of gradient magnitudes is only loosely tied to underlying DSMC simulation accuracy, for which collision separation is far more consequential than sampling grid resolution. In any case, trends and quantities in Figure 5 should be roughly accurate to within an order of magnitude outside the shock and the Knudsen layer along the wall. The Knudsen layer is in turn defined by the condition $\delta/\lambda \lesssim 1$ where δ denotes distance from the wall.

To more easily assess the extent of continuum breakdown for the baseline case, and to determine the influence of crossflow and sweep on continuum breakdown for the conditions of interest, gradient length Knudsen numbers $Kn_{GLL,q}$ along the stagnation streamline are plotted in Figure 6 for the baseline simulation as well as for the "no crossflow" and "no sweep" simulations. In interpreting the results in Figure 6, it should be noted that any apparent trends for $Kn_{GLL,q} < 10^{-4}$ should be discounted due to the influence of statistical scatter effects. It follows that measurable degrees of nonequilibrium along the stagnation streamline are found only within a small distance of the shock and boundary layer. For the baseline case, near the stagnation point the velocity-based Knudsen number is considerably larger than the pressure and density-based Knudsen numbers, indicating the dominant influence of the velocity gradient on translational nonequilibrium in this region. However, Figure 6 shows that the velocity-based Knudsen number becomes negligibly small near the stagnation point in the absence of either crossflow or sweep.

In Figure 7, surface momentum fluxes are plotted as a function of cylinder angle θ relative to the x-axis. Results from all three simulations are included for surface pressure, shear stress magnitude, and shear stress components in the z (or crossflow) direction and along the x-y plane. To reduce statistical scatter and more easily visualize trends, post-processing smoothing operations were applied to all surface quantities except pressure in these and subsequent plots from the two-dimensional DSMC simulations. Baseline simulation results in Figure 7 show that the dominant contributor to shear stress, especially for small θ, is in the crossflow direction. In contrast, a comparison of pressure curves from the three simulations indicates that crossflow has an almost negligible impact on surface pressure for the conditions of interest. In comparing results between the three cases, shear stress in the x-y plane is found to be strongly dependent on sweep but nearly independent of crossflow.

Figure 8 shows the variation with θ in surface heat flux for the three two-dimensional DSMC simulations. As expected due to the much greater shock strength in the absence of sweep, the "no

sweep" case shows considerably higher surface heating than the baseline case. For the "no crossflow" case, the heat flux is uniformly negative at the prescribed wall temperature, and the difference between values for this case and those for the baseline case represent the influence of crossflow-induced viscous dissipation within the boundary layer. It should be noted that the increased surface heating due to viscous dissipation only partially makes up for the heating reduction associated with a weaker bow shock in the presence of sweep.

Wall temperature jump and slip velocity magnitude are plotted as functions of θ in Figure 9. Results are shown for both translational and rotational temperatures, and the prescribed wall temperature is denoted by dashed horizontal lines. (Vibrational temperatures at the wall are subject to much greater statistical scatter, and are excluded from Figure 9 due to the difficulty of identifying any definite trends.) Temperature jump – defined as the difference between local gas temperature and wall temperature – and velocity slip are two recognized consequences of near-wall rarefaction or thermal nonequilibrium in high speed flows, and both quantities are known to have potentially significant influence on surface heating prediction. In a finding which is consistent with heat flux results in Figure 8, the presence of crossflow is shown in Figure 9 to lead to a sign reversal in wall temperature jump for both translational and rotational temperatures. Surprisingly, due to competing effects of reduced wall temperature gradients and increased rarefaction effects associated with lower bow shock strength, the baseline case is shown to have roughly comparable temperature jump to the "no sweep" case. Similarly, wall velocity slip is found to be comparable for the "no crossflow" and "no sweep" cases, as the impact of lower wall velocity gradients for the "no crossflow" case is roughly cancelled by the increase in near-wall rarefaction effects due to reduced gas density. Slip velocity magnitudes for the baseline simulation are found, however, to be uniformly higher than those for the other two simulations, primarily due to the nonzero crossflow component in the slip velocity vector.

Figure 10 shows the variation with θ in local Knudsen numbers along the wall which are computed as functions of surface quantities. Due to limitations on the accurate calculation of gradient-based Knudsen numbers along the wall, which are in turn attributed to a combination of statistical scatter effects and characteristic length scales that may be much smaller than DSMC sampling cell dimensions, continuum breakdown may be more easily computed within the Knudsen layer from a DSMC simulation through the use of surface quantities such as wall temperature jump. In earlier work [20], a series of continuum breakdown parameters were derived as functions of wall pressure, slip velocity and temperature jump. These parameters are defined as follows:

$$Kn_{wall,p} \equiv \left(\frac{2\alpha}{2-\alpha}\right)\left(\frac{\gamma+1}{9\gamma-5}\right)\left|\left(\frac{2}{\alpha}\left(\frac{p_{flux}}{p_{scalar}}-1\right)+1\right)^2-1\right| \tag{2}$$

$$Kn_{wall,T} \equiv \left(\frac{2\alpha}{2-\alpha}\right)\left(\frac{\gamma+1}{9\gamma-5}\right)\left|\frac{\Delta T}{\Delta T+T_{wall}}\right| \tag{3}$$

$$Kn_{wall,V} \equiv \left(\frac{\alpha}{2-\alpha}\right)\frac{V_{slip}}{\sqrt{\gamma R(\Delta T+T_{wall})}} \tag{4}$$

where Eqs. (2), (3) and (4) give the pressure, velocity and temperature parameters, respectively. Here α is the wall thermal accommodation coefficient (defined for the Maxwell model [13] as the probability that a gas molecule colliding with a wall will experience diffuse reflection at the wall temperature, as opposed to specular reflection, and equal to 1 in this work), γ (set to 1.4 here for post-processing calculations) is the specific heat ratio, p_{flux} is the surface pressure computed from the wall-normal momentum flux, p_{scalar} is the scalar pressure based on the translational temperature and density in the wall-bounded sampling cell, ΔT is the wall temperature jump for either translational or rotational temperature, T_{wall} is the wall material temperature, V_{slip} is the slip velocity magnitude, and R is the specific gas constant. The parameters $Kn_{wall,p}$, $Kn_{wall,T}$ and $Kn_{wall,V}$ are used to assess wall continuum breakdown based on pressure (or normal momentum flux) anisotropy, temperature jump and velocity slip, respectively. Following the derivation of these parameters from gradient-based Knudsen numbers as given by Eq. (1), continuum breakdown is

assumed when any parameter – excluding $Kn_{wall,T}$ for rotational temperature, which is associated with rotational nonequilibrium – exceeds a threshold value of 0.05. Given the approximate nature of the analysis, continuum breakdown is also considered probable when any of these parameters approaches the threshold value. This threshold is denoted in Figure 10 by dashed horizontal lines.

Results for all three cases in Figure 10 suggest that continuum breakdown associated with pressure anisotropy may occur near the stagnation point at $\theta = 0°$. For the baseline case, the slip velocity parameter indicates that continuum breakdown may in fact occur over the entire surface, based on a more conservative notional threshold of 0.02. In contrast, for the other two cases the slip velocity parameter is found to be far out of range of values that may indicate continuum breakdown, except near the outflow boundary at $\theta = 90°$ where an unphysical expansion effect is likely present around the narrow subsonic boundary layer region. In comparing the "no sweep" results in Figure 10 to those for the baseline simulation, it is observed that sweep has little impact on near-wall nonequilibrium as measured by either the pressure anisotropy, translational temperature, or rotational temperature parameters.

COMPARISON WITH EXPERIMENT

Given the lack of a converged three-dimensional DSMC solution for the geometry and experimental conditions of Bushnell [8], no direct assessment of DSMC simulation accuracy can be performed based on the available experimental data. However, an indirect comparison with experimental data is still possible, by assuming that the baseline surface pressure and heat flux at $\theta = 0°$ should match experimentally measured stagnation line values (i.e., values at the intersection of the symmetry plane and cylinder forebody surface) at a large distance from the wedge. More specifically, measurement locations should be sufficiently far from the wedge to largely avoid any influence of either the shock-shock interaction or spanwise shock layer development along the cylinder.

In Figure 11, the surface pressure at $\theta = 0°$ from the baseline simulation (represented by the blue horizontal line) is displayed on a plot of experimentally measured stagnation line pressure, normalized by freestream total pressure, from Ref. [8]. Horizontal axis values in the figure are given by the axial distance, L, from the cylinder end, normalized by the cylinder diameter, D. Unfortunately, no published results are available for pressure at the laminar flow conditions of interest in the present work ($Re_D = 8.9\times10^4$), and experimental data is therefore plotted for higher Reynolds number conditions ($Re_D = 1.92\times10^5$) at which the cylinder boundary layer was found to be predominantly turbulent. Approximate locations of the shock intersection and the shock-interaction-induced expansion wave impingement on the cylinder, as provided in the published results of Bushnell [8], are represented in the figure by vertical green lines.

Figure 11 also includes two sets of N-S simulation results. FUN3D was used to perform a RANS simulation of fully turbulent flow at the $Re_D = 1.92\times10^5$ test conditions, with the one-equation Spalart-Allmaras turbulence model and local time-stepping. An unstructured grid, generated in Pointwise based on the experimental geometry, includes highly stretched hexahedral-dominant near-wall cell layers, and is refined such that the cell size parameter y^+ which is uniformly less than 0.5 along wall boundaries. A second FUN3D simulation was also performed using the same grid, with turbulence disabled, at the $Re_D = 8.9\times10^4$ conditions corresponding to the DSMC simulation.

Normalized pressure results from both FUN3D simulations included in Figure 11 show very good agreement with each other, as well as reasonably good agreement with the experimental data. In particular, normalized pressures downstream of the shock intersection point generally (though not universally) fall within the small experimental error bounds, and the regions of expansion-induced pressure drop are relatively close between the measured data and both sets of N-S results. Moreover, the N-S results appear consistent with an assumption that normalized surface pressures vary little with Re_D for the geometry and flow conditions of interest, and an assumption that stagnation line pressure asymptotically levels off at large distances from the wedge. Given these observations, the relatively good agreement between experimental data and

Re_D = 1.92×10^5 N-S results, coupled with the excellent agreement between the two sets of N-S results, allow the experimental data in Figure 11 to be used indirectly as a measure of accuracy for the DSMC surface pressure at θ = 0°. This DSMC pressure value is nearly coincident with the Re_D = 8.9×10^4 N-S values at large L/D. It follows that a comparison of results in Figure 11 supports a finding of acceptable solution accuracy in the baseline DSMC simulation.

While results shown in Figure 11 are encouraging, surface pressure is known to be relatively tolerant of numerical errors in high-speed flow simulations, so only limited conclusions can be drawn from pressure comparisons such as these. In contrast, surface heat flux – which in DSMC is computed as an often-small difference between comparatively large incident and reflected energies during particle-wall collisions – tends to be highly sensitive to numerical errors and input biases. In Figure 12, the normalized convective heat transfer coefficient along the stagnation line is presented from experimental measurements at Re_D = 8.9×10^4 and from the laminar FUN3D simulation at the same flow conditions, with the corresponding two-dimensional DSMC value denoted by the blue horizontal line. The normalized heat transfer coefficient $\bar{h}$ is proportional to the surface heat flux $\dot{q}''$, and is given for laminar flow by

$$\bar{h} = \frac{\dot{q}''}{h_{ref}} \left(T_\infty \left(1 + Pr^{1/n} \left(\frac{\gamma - 1}{2} \right) M_\infty^2 \right) - T_{wall} \right)^{-1} \quad (5)$$

where h_{ref} = 2.042 W/cm^{2}K is a reference heat transfer coefficient for the Re_D = 8.9×10^4 case, T_∞ = 54.2 K is the freestream temperature, M_∞ = 7.95 is the freestream Mach number, Pr = 0.72 is the Prandtl number, n = 2 for laminar flow, and T_{wall} = 310.9 K is the wall temperature.

Relative to the experimental data points, significant overestimates in N-S results are found in Figure 12, with discrepancies in the range of 20% for L/D < 2. A comparison of N-S heating results at large L/D with the DSMC heating value show discrepancies of roughly 10%, where higher values are found from the N-S simulation. It follows that heating coefficients more consistent with the DSMC value (i.e., lower than that found from the N-S solution) would be expected if experimental data was taken for higher L/D. One possible contributor to the likely overestimate in N-S heating predictions is the influence of thermal nonequilibrium effects – specifically wall temperature jump and velocity slip – which are associated with near-wall continuum breakdown predicted through the above analysis of DSMC results. Furthermore, to the extent that the DSMC $\bar{h}$ value shown in Figure 12 provides an overestimate in comparison to the experiment (following extrapolation of measured data to larger L/D), this overestimate may be at least partly attributed to the choice of thermal accommodation coefficient α for DSMC modeling of gas-surface interaction. While molecular beam experiments and other historical studies have shown that α may depend strongly on temperatures, gas species, surface material and surface roughness, values closer to 0.9 than 1 (as assumed here) have often been used under relevant conditions in the literature. An overprediction by around 10% in α then roughly corresponds to DSMC-based surface heating overestimates in the range of 10%, as is found here. Such an explanation is far from conclusive, but it does at least suggest one contributing factor to the observed discrepancies.

THREE-DIMENSIONAL NONEQUILIBRIUM ANALYSIS

As discussed above, three-dimensional DSMC simulation for the geometry and flow conditions of the Bushnell experiments [8] are extremely challenging, and given limitations on available tools and computing systems, attempts to generate converged three-dimensional DSMC solutions for comparison with data from these experiments were unsuccessful. In particular, even while employing several strategies to reduce computational expense, the total expense for one such solution was estimated to be on the order of tens of millions of CPU hours. However, flight-relevant conditions with considerably higher global Knudsen numbers, Kn, can be simulated at greatly reduced expense. In fact, the global Kn (based on cylinder diameter) of around 1.6×10^{-4} for the flow conditions of the baseline two-dimensional DSMC simulation is found to be roughly 20 times lower than that expected at flight-relevant conditions. It can be shown that computational

expense for three-dimensional DSMC simulations should scale roughly with Kn^{-4} (where Kn^{-3} scaling is associated with collision separation or cell size requirements, while Kn^{-1} scaling occurs in the number of time steps during the transient startup period). Thus, even accounting for the highly imprecise and speculative nature of this scaling analysis, a three-dimensional DSMC simulation based on the geometry of Bushnell but at flight conditions is conservatively predicted to require only hundreds to thousands of CPU hours. This finding of feasible computational expense, along with an expectation that thermal nonequilibrium effects are stronger at the higher Kn and higher enthalpies expected around a swept wing leading edge in hypersonic flight, motivates consideration of flight conditions in place of experimental conditions for three-dimensional DSMC analysis.

The following flight conditions and geometry are employed here, and are considered representative of those expected for a hypersonic cruise vehicle: A wing leading edge has a 60° sweep (consistent with the Bushnell experiment) and a curvature radius of 0.03 inches, following the initial leading edge design for the X-43A hypersonic demonstrator [21]. The freestream dynamic pressure is 800 psf, as estimated to satisfy scramjet operability constraints, and the freestream Mach number (again based on the Bushnell experiment) is 7.95. These freestream conditions correspond to an altitude of about 68,700 ft, a global Knudsen number $Kn = 2.88\times10^{-3}$ and a Reynolds number $Re_D = 3.36\times10^{3}$.

SIMULATION SETUP

DSMC simulations are performed using diffusely reflecting isothermal wall boundaries, with wall temperature based on expected leading edge material tolerances. Three different wall temperatures are used, corresponding to different possible materials and cooling strategies. One simulation is run with the wall temperature set to 1200 K, based on the operational temperature limit for Inconel 625. This material is thought to be potentially viable at conditions of interest, especially when used in combination with planar heat pipes or other active cooling techniques [22]. Additional simulations use wall temperatures of 1800 and 2400 K, which would be suitable for coated C-C substrate or ultra-high temperature ceramics such as HfB_2. For traceability to the Bushnell experiment, while preserving the global Kn, Re and freestream Mach number from the flight conditions outlined above, the Bushnell experiment geometry for the 60° separated cylinder is used and simulation input and output quantities are appropriately scaled. In particular, the freestream density is scaled by the ratio (0.06) of desired leading edge curvature radius to cylinder radius, while heat flux and other density-dependent output quantities are multiplied by the reciprocal of this ratio. Simulations are performed for five-species (N_2, O_2, N, O and NO) reacting air, with the quantum kinetic model of Bird used for dissociation, recombination, exchange reactions, and vibrational exchange probabilities [23]. Note that although the freestream total temperature (3043 K) is in the general range for which some limited O_2 dissociation may be expected, air chemistry effects have in fact been found to be negligible here, and air chemistry models are enabled but not actually used in the calculations. Other DSMC physical models, such as the variable hard sphere collision model [13], are the same as those described above for the two-dimensional simulations.

Although the flight conditions of interest are not prohibitively expensive for DSMC, efficient DSMC simulation within the limits of available resources is still a challenge for this case. A series of complementary strategies are therefore used to improve efficiency while adhering to standard guidelines for DSMC accuracy. One such strategy involves dramatically reducing the simulation domain size, in both longitudinal and transverse directions, by excluding from the domain the wedge which was used by Bushnell to generate an incident oblique shock. The incident shock is instead generated along an upstream edge of the cuboidal simulation domain, by assigning different inflow conditions to the two sides which share this edge. While one set of inflow conditions is taken from the freestream conditions, the other is computed as a function of the wedge angle using oblique shock relations. The cylinder is then repositioned so as to preserve its location with respect to the incident shock, neglecting the small influence of boundary layer development and other viscous interactions around the wedge.

Another strategy employed here to improve efficiency is the use of collision limited DSMC outside a small region surrounding the cylinder shock layer [24]. This method involves unphysically imposing a near-equilibrium velocity distribution, as a diffusive means of simulating an inviscid flow. In the unique collision limiter implementation of the HAP code, near-neighbor collision partner selection is efficiency applied via transient adaptive subcells, and internal energy (translational-rotational and translational-vibrational) exchange rates are determined from the local equilibrium collision frequency.

Outside the collision limiter domain, around the shock layer surrounding the cylinder, DSMC collision partners are selected using a one-dimensional sorting routine [24]. Particles within each cell are rapidly sorted in the local surface-normal direction – which is generally aligned with the dominant gradient direction – and particle pairs are then preferentially selected to minimize collision separation in this direction while avoiding repeated selection of identical pairs. A unique collision probability adjustment in HAP allows this probability to vary across the volume of individual cells according to intra-cell density variation. This adjustment allows for collision cell dimensions larger than the local mean free path, and when combined with one-dimensional sorting, an effect similar to cell stretching on body-fitted grids may be obtained using a Cartesian cut-cell grid [24].

Another strategy utilized here to reduce simulation expense is the use of dynamic local time step adaptation. Outside of the collision limiter domain, the time step interval is periodically adapted to a uniform fraction (1/5) of the mean collision time in each cell. This serves two purposes: (1) avoiding unacceptably large time steps that would violate assumptions underlying an operator splitting approach to the governing Boltzmann equation, and (2) preferentially increasing particle populations in high-density regions where DSMC collision separation requirements are most difficult to satisfy. Within the collision limiter domain, the time step interval is scaled with density gradient magnitude, as a means to selectively increase particle populations in high-gradient regions. When combined with near-neighbor collision selection, this should improve resolution of shocks and other inviscid flowfield structures.

The three-dimensional DSMC simulations use approximately 10 million particles at steady state, and employ time-averaged sampling over 100,000 time steps following a 100,000 step transient startup period. Each simulation requires about 1100 CPU hours on the NASA Pleiades high performance computing system.

SIMULATION RESULTS

A synthetic Schlieren image is presented in Figure 13. The image is generated from contours of longitudinal density gradient magnitude along the symmetry plane for the case with T_{wall} = 1200 K. (On the scale of this figure, results from the three three-dimensional DSMC simulations have negligibly small differences outside of statistical scatter. The same case is therefore used for all other contour plots in this section.) Clearly visible flow structures include the incident shock, the bow shock along the cylinder, low-density expansion regions in the wake and below the cylinder end-plate, and a shear layer (between the bow shock and cylinder) created by an Edney Type VI shock-shock interaction [1], as illustrated in Figure 1. An expansion fan that is also created by this interaction, which is not observable with the color map used to differentiate other flowfield features, lies within the black region along the forebody cylinder surface.

Contours of normalized pressure along the symmetry plane and cylinder surface are shown in Figure 14. In Figure 15, Mach number contours are shown along the symmetry plane, and heat flux is displayed on the surface. To better illustrate surface properties, black lines at numbered contour levels are included in these figures for the surface pressure and heat flux. Surface heat flux contours in Figure 15 indicate a large increase in heating due to the influence of the wedge (which is not explicitly modeled here but is represented by post-shock inflow conditions), but there is no noticeable heating spike associated with the shock-shock interaction. This finding is consistent with a Type VI shock-shock interaction, for which the only associated structure that impinges on the surface is a centered expansion fan. As shown in Figures 14 and 15, the drop-off in surface

heating, as well as in surface pressure, near the shock-shock interaction is attributed to this impinging expansion fan.

In Figure 16, contours are shown along both the symmetry plane and cylinder surface for gas translational, rotational and vibrational temperatures. Note the large gradients in translational and rotational temperatures along the shear layer downstream of the shock-shock interaction, as expected due to density variation across the shear layer in an interaction of Type VI. Also note the discontinuity in wake rotational temperature near the outflow boundary. This discontinuity is located along the border between conventional DSMC and collision limited DSMC domains, and is attributed to an equilibrium approximation used in collision limiter operations to determine translational-rotational energy exchange probabilities. In comparing vibrational temperature to the other two temperatures across the shear layer in Figure 16, strong vibrational nonequilibrium or vibrational freezing is observed. This trend is a consequence of comparatively large vibrational collision numbers, which vary (as computed using the quantum kinetic model of Bird [23]) with species and location but are generally an order of magnitude greater than rotational collision numbers. Some rotational freezing, indicated by discrepancies between rotational and translational temperatures, is also noticeable within the forebody boundary layer and throughout the wake.

Figure 17 includes two different contour views for the maximum gradient length local Knudsen number $Kn_{GLL,max}$ and the wall slip velocity magnitude V_{slip}. As discussed above in reference to the two-dimensional DSMC analysis, continuum breakdown is generally assumed for $Kn_{GLL,max} \gtrsim 0.05$, and conditions approaching or exceeding the approximate 0.05 threshold are found within the shocks, wake regions and forebody boundary layer. Significant slip velocity – another indicator of continuum breakdown or rarefaction effects – is observed across the cylinder, with especially large values along the lateral and aftbody surface regions.

In Figure 18, surface heat flux and pressure along the stagnation line (where the forebody surface intersects the symmetry plane) are plotted for all three cases with T_{wall} = 1200, 1800 and 2400 K. The pressure curves indicate that wall temperature has very little impact on surface pressure, with nearly coincident results showing a sharp drop across the expansion impingement region, followed by a gradual pressure increase with progressively decreasing slope. The heat flux is shown to be consistently near zero for the 2400 K case, and this temperature can therefore be considered representative of adiabatic leading edge conditions. Note that, for a wing leading edge in flight, lower temperatures would be expected – at least outside any bow shock overlap region corresponding to the region affected here by the wedge – due to the combined influence of radiative cooling and conductive heat transfer through the leading edge material. The heat flux contours for T_{wall} = 1200 and 1800 K cases show considerable heating augmentation from the influence of the wedge and the protruding cylinder end-plate, but no spike associated with shock-shock interaction. As described above in the discussion of Figure 15, this observation is consistent with expected trends for an Edney Type VI interaction [1].

In interpreting heat flux trends from Figure 18, it should be emphasized that the non-localized heating augmentation (discounting the end-plate associated spike around L/D = 0) downstream of the wedge post-shock region is a consequence of the presence of the wedge but not the wedge shock itself. More specifically, a streamtube through the cylinder shock that also crosses the wedge shock will have a comparatively large freestream capture area due to compression across the wedge shock. As a consequence, this streamtube tends to hold a greater integrated total enthalpy flow rate than a streamtube of equal area within the cylinder shock layer which has not passed through the wedge shock. The end result of this elevated total enthalpy flow rate is an increase in heating along the adjacent surface region, as found in Figure 18 near the cylinder end. This effect can be more simply characterized as a concentration of flowfield energy due to wedge shock compression.

Figure 19 shows an estimate of the stagnation line temperature distribution for a radiative equilibrium wall, where the blackbody radiative heat flux is equal to the convective heat flux, and where any shock layer emission and internal conduction or conjugate heat transfer effects are neglected. Given the stochastic nature of DSMC and the resulting difficulty in dynamically varying

local wall temperature based on computed heat flux, the results in Figure 19 are estimated from the simulation with an isothermal wall temperature of T_{wall} = 1800 K. This case was chosen because, over much of the cylinder length, the estimated radiative equilibrium wall temperatures T_{radeq} shown in Figure 19 are relatively close to the prescribed temperature T_{wall}. These temperatures are computed using the energy balance $\dot{q}" = \epsilon\sigma T_{radeq}^4$ where $\dot{q}"$ is the local wall heat flux from the DSMC solultion, ϵ = 1 is the blackbody emissivity as desired to maximize radiative cooling, and σ is the Stefan-Boltzmann constant. This estimation procedure is in fact equivalent to the first iteration in the standard iterative procedure to calculate T_{radeq} during a deterministic CFD simulation, and the estimation accuracy is therefore strongly dependent on the difference between T_{radeq} and T_{wall}. It follows that results in Figure 19 should not be viewed with a high degree of confidence, especially upstream of the expansion impingement region for L/D < 2, but these results do at least provide a general indication of expected temperatures for a poorly conducting leading edge material. As shown in the figure, the stagnation line radiative equilibrium wall temperature drops by at least a few hundred degrees across the expansion wave impingement zone around L/D ≈ 2, to a value in the range of 1800 K, then gradually increases from that value with downstream distance. Wing leading edge temperatures around 1800-2000 K could be safely assumed in the absence of an impinging bow shock.

In Figure 20, wall temperature jump is plotted along the stagnation line as a function of normalized distance L/D for translational, rotational and vibrational temperatures, for the three different T_{wall} cases. Very high levels of statistical scatter are shown in the figure, due in part to the relatively small temperature jump values in comparison to the temperature variation across the flowfield. (For example, as one predictive metric for comparatively large scatter effects in DSMC, temperature jump values tend vary between one and two orders of magnitude below absolute temperatures near the wall.) As expected, the wall temperature jump is generally found in Figure 20 to decrease as the wall temperature increases. This trend, while arguably counter-intuitive here, would be obvious for specularly reflecting or adiabatic surfaces where the wall temperature has no influence on the gas temperature at the wall; for such cases a higher wall temperature T_{wall} must by definition correspond to a smaller temperature jump.

Another observation from Figure 20 is that curves for all three cases are within a relatively small range. This is attributed to competing effects of surface heat transfer and density variation within the boundary layer. More specifically, temperature jump magnitudes are comparable because, as wall temperature increases, effects of reduced heat flux are countered by the impact of a larger mean free path (which is approximately inversely proportional to density) along the wall. The increase in mean free path in turn leads to stronger rarefaction effects including temperature jump. An additional trend shown in Figure 20, which may be distinguished from the high level of considerable scatter, is that vibrational gas temperatures along the wall are lower than the wall temperature (corresponding to negative vibrational temperature jump), which is likely associated with partial vibrational freezing across the boundary layer. In contrast, rotational and translational temperatures are consistently greater than the wall temperature for the T_{wall} = 1200 and 1800 K cases, indicating positive contributions to the wall heat flux. For the case with T_{wall} = 2400, translational and rotational heat flux contributions along the stagnation line are found to generally be positive and negative, respectively, with the two contributions largely cancelling each other out and leading to the small heat flux magnitudes shown in Figure 18.

Wall slip velocity magnitudes along the stagnation line are plotted for the three T_{wall} cases in Figure 21. The figure shows sharp spikes in slip velocity around both the cylinder end at L/D = 0 and the outflow boundary. The cylinder end spike is attributed at least in part to the influence of a strong expansion region generated around the end-plate leading edge, while the downstream spike is likely caused by the unphysical influence of a supersonic outflow boundary condition within the near-wall region where subsonic flow is expected. Away from these spikes, roughly uniform slip velocity (within the large degree of statistical scatter) is found for all three cases, with values that tend to increase at higher T_{wall} due to the corresponding increase in local mean free path.

In Figure 22, local Knudsen numbers based on wall quantities, as defined in Eqs. (2)-(4), are plotted along the stagnation line for each T_{wall} case. The continuum breakdown threshold at Kn = 0.05 is denoted in each plot by a dashed horizontal line. Note the high level of scatter in the Knudsen number $Kn_{wall,p}$ based on pressure anisotropy, as follows from the very small sampling sizes associated with cell-averaged quantities (translational temperature and density) used to compute scalar pressure along the wall. For the T_{wall} = 1200 K case, a comparison of Kn curves with the breakdown threshold suggests that continuum breakdown occurs over much or all of the stagnation line, due to the influence of both slip velocity and pressure anisotropy. In contrast, rotational nonequilibrium along the stagnation line is shown by the temperature jump parameter to be comparatively weak. For the T_{wall} = 1800 and 2400 K cases, continuum breakdown is predicted over nearly the entire stagnation line – with the possible exception of the L/D < 2 region upstream of the expansion wave impingement – as indicated by the slip velocity parameter. Together with Figure 17, the results in Figure 22 appear to show that continuum breakdown can occur around the wing leading edge under representative hypersonic flight conditions, although the extent of continuum breakdown may depend little on the presence of an impinging bow shock. This has potential implications on the accuracy of leading edge aerothermal analysis based on N-S simulation, but the quantitative influence of invalid N-S approximations on heating predictions under relevant conditions are currently unclear.

NAVIER-STOKES ANALYSIS OF TURBULENT EXPERIMENTAL CONDITIONS

To complement the DSMC-based nonequilibrium analysis presented above for low-Re_D laminar conditions, another component of this work involved RANS CFD simulation of the Bushnell experiment at higher Re_D conditions for which the flow was found to be predominantly turbulent [8]. The cylinder-wedge geometry used for RANS analysis, as for the DSMC analysis above, was modeled after the separated 60° cylinder case from Bushnell [8]. The schematic in Figure 23 shows the computational domain of the cylinder-wedge model. The cylinder and wedge both use wall boundaries with the no-slip condition applied. Additionally, the wall surface temperatures are set to 311 K following the estimate of Bushnell [8]. The wedge angle is 12° and there is an elliptical end-plate on the bottom end of the cylinder that is oriented parallel to the wedge. Two symmetry boundary conditions are employed: 1) a z-symmetry at the minimum z value, corresponding to the cylinder centerline, and 2) a y-symmetry plane at the minimum y value, which is the small region forward of the wedge leading edge. An inflow boundary condition is imposed on x-plane forward of the wedge leading edge and an outflow pressure boundary is imposed on the furthest aft x-plane. The z-plane at the maximum z value is set to a tangency boundary condition and the y-plane at the maximum y value is set to a farfield boundary condition.

A hybrid hex-prism-tet grid was used for this study. Hex and prism elements were used to resolve the boundary layers to provide good quality heating calculations. Also, volume source terms were used to help resolve the oblique shock formed from the wedge as well as the cylinder bow shock. The steady, compressible, RANS version of FUN3D [14] was used to perform the calculations. The flow was assumed to be calorically perfect. The inviscid fluxes were constructed using a hybrid scheme that employs the van Leer Scheme for shocks and the low dissipation flux splitting scheme (LDFSS) near walls. The van Albada limiter was also used. The Menter shear stress transport (SST) two-equation turbulence model with strain source term was used for the turbulent flow cases.

A grid convergence study was performed to ensure grid independence. A turbulent flow case with a freestream Mach number of 7.95 and a Reynolds number Re_D based on the cylinder diameter of 2.85×10^5 was used to perform the grid convergence study. Figure 24 shows the normalized heat transfer coefficient along the centerline of the cylinder. The heat transfer coefficient is normalized with respect to a reference heat transfer coefficient of 2.042×10^4 W/m^{2}K. Also, to estimate the adiabatic wall temperature required to compute the heat transfer coefficient, the recovery factor was assumed to be the Prandtl number to the 1/3 power and the Prandtl number to the 1/2 power for turbulent and laminar flow respectively. In both cases, the Prandtl number is

assumed to be a constant value of 0.72. The length along the centerline of the cylinder in normalized with respect to the cylinder diameter. Three levels of grid refinement were studied: a coarse, medium, and fine grid. The coarse grid contains approximately 21 million cells, the medium grid contains approximately 30 million cells, and the fine grid contains approximately 72 million cells. For all three levels of grid refinement shown in Figure 24, the initial boundary layer cell height is held constant at 2.0×10^{-4} inches. The increased grid resolution was obtained by decreasing the average cell size on the cylinder surface mesh and by decreasing the average cell size within the volume source terms placed in the vicinity of where the oblique shock from the wedge intersects the bow shock from the cylinder. The results in Figure 24 show good agreement between the medium and fine mesh. For the same three grids, Figure 25 shows the pressure, normalized with respect to the freestream total pressure, along the cylinder centerline or stagnation line. Again, there is good agreement between the medium and fine mesh.

To ensure adequate grid resolution within the boundary layer, and to again ensure grid independence, several different initial boundary layer cell heights were studied. In each case, the cell growth rate was fixed at ten percent. Figure 26 shows the normalized heat transfer coefficient along the cylinder centerline for three different initial boundary layer cell heights. Note that the results shown in Figure 26 are for the coarse surface mesh presented in Figures 24 and 25. Similar results are shown in Figure 27 for two different initial boundary layer cell heights but for the fine surface mesh instead of the coarse surface mesh. The results in Figures 26 and 27 are in good agreement with each other.

The Mach contours on the center plane for the turbulent flow FUN3D simulation are shown in Figure 28, along with contours of the heating on the cylinder surface. The flowfield is consistent with the schematic shown in Figure 1. There is an expansion fan emanating from the intersection point and a shear layer can also be seen in Figure 28. Note that most of the increased heating effects on the cylinder surface occur forward of the expansion impingement point.

Figure 29 shows a comparison between the heating predicted by the CFD results and the experimental data for two different flow conditions, a laminar case with $Re_D = 8.9\times10^4$, and a turbulent case with $Re_D = 2.58\times10^5$. For both cases, the freestream Mach number is 7.95. The error bars displayed in Figure 29 are based on Bushnell's prediction of a 15 percent error for the heat transfer data.

Two points are included in Figure 29, the shock intersection point and the expansion impingement point. The CFD result for both the laminar and turbulent cases overpredict the heating at L/D values below about 1.5. One possibility for this discrepancy is the selected turbulence model, however, the fact that the same discrepancy also exists in the laminar case, which Bushnell identifies as a fully laminar flow case, points to a different explanation. Another possibility for the discrepancy could be due to a discrepancy between the alignment of the elliptical end plate in the CAD model versus the actual experiment. The hybrid hex-prism-tet grid might also be inadequate to capture the true heating values in this complex flow region, where a structured grid might instead be more appropriate.

The pressure along the cylinder for the turbulent flow case ($Re_D = 2.58\times10^5$) is shown in Figure 30. The pressure is normalized with respect to the freestream total pressure. Also shown in Figure 30 are experimental data from Bushnell for different Reynolds numbers, one value above the CFD case, and one value below the CFD case. The error bars corresponding to the experimental data are based on an estimation by Bushnell of a five percent error for the pressure data captured during the experiment. The shock intersection point and the expansion impingement point are also included in Figure 30.

SUMMARY AND CONCLUSIONS

A combination of DSMC and N-S CFD analysis has been used to investigate aerothermal processes and phenomena related to incident shock impingement on a highly swept leading edge, with implications for wing leading edge heating on a hypersonic cruise vehicle. A series of

simulations were performed to determine surface heat transfer and assess shock layer thermal nonequilibrium effects for an inclined cylinder in the presence of a shock-generating ramp, at conditions around Mach 8 based on historical experiments of Bushnell [8] for an Edney Type VI shock-shock interaction. Unlike the more thoroughly studied shock interaction types (e.g., Type IV) for which intense local surface heating augmentation is expected, Type VI interactions are not characterized by a surface heating spike, and any leading edge design considerations (materials selection, leading edge curvature, thermal management strategy, etc.) should properly account for the presence of this interaction type.

Two-dimensional DSMC simulations were run at experimental conditions for which three-dimensional DSMC analysis of the shock-shock interaction was found to be prohibitively expensive, while three-dimensional DSMC simulations were performed at computationally challenging but feasible flight-representative conditions. Nonequilibrium effects associated with wall velocity slip, pressure anisotropy, and temperature jump were quantified, and near-wall continuum breakdown was observed for both experimental and flight conditions.

One important observation from this analysis is that, at conditions of interest, increased surface heating due to crossflow-induced viscous dissipation makes up a significant fraction of the heating reduction associated with reduced bow shock strength over a swept leading edge. Reasonably good agreement was found through an indirect comparison of two-dimensional DSMC results and experimental data, with uncertainty in the DSMC thermal accommodation coefficient identified as one contributor to observed discrepancies in surface heating rates. At flight conditions, a rough estimate of radiative equilibrium wall temperature indicated stagnation line temperatures in the range of 1800 K, and significantly elevated temperatures were found in the region downstream of an incident (wedge-generated) shock. Surprisingly, temperature jump values were shown to be only weakly dependent on the prescribed isothermal wall temperature, as the influence of increased convective heating at lower wall temperatures was countered by a corresponding reduction in the mean free path along the wall.

The incident shock impingement on a swept cylinder was also studied using N-S CFD analysis, which would likely be considered the standard engineering practice in today's environment. The anticipated flow features of an Edney Type VI shock-shock interaction were clearly visible from the CFD results. Also, as expected, the expansion waves emanating from shock-shock intersection point do not result in enhanced heating on the cylinder at the location where the waves impinge on the surface; instead, the enhanced heating is observed on the cylinder surface forward of the impingement point. While the qualitative aspects of the flowfield were easily resolved using N-S CFD, the quantitative surface heating predictions could still be improved when compared to experimental data. It is likely that the nonequilibrium effects highlighted through the DSMC analysis could account for part of the discrepancy between the CFD results and the experimental data.

In an overall assessment of results from this study, it can be stated that generally favorable comparisons with experiment provide confidence in the accuracy of simulation results, and these results in turn suggest the importance of various nonequilibrium processes and phenomena. Further work, possibly involving detailed comparisons from DSMC and laminar N-S simulations with identical physical models and flow conditions, would be required to quantify the influence of nonequilibrium effects for the class of leading edge shock interaction problems considered here. Other prospective future work would be needed to evaluate the sensitivities of observed flowfield and surface characteristics to geometric inputs (e.g., sweep angle, leading edge curvature radius, and incident shock strength) as well as freestream parameters such as Mach number, dynamic pressure and total ethalpy. More generally, it is hoped that the present work provides valuable physical insight and improved quantitative understanding for shock interference heating on a swept leading edge in hypersonic flow, specifically for Type VI shock-shock interactions relevant to flight conditions around the wing leading edge on a hypersonic cruise vehicle. Possible outcomes include increased confidence in predictive capabilities for aerothermal analysis of hypersonic cruise vehicles, with a corresponding reduction in leading edge heat load margins. Study results could

potentially influence design decisions for future hypersonic vehicles, with implications related to materials selection, leading edge thickness and thermal management.

REFERENCES

[1] Edney, B. E., "Effects of Shock Impingement on the Heat Transfer around Blunt Bodies," AIAA Journal, Vol. 6, No. 1, 1968, pp. 15-21.

[2] Sobel, D., "Cowl Leading Edge Heat Transfer in the Presence of Shock Impingement," AIAA paper 90-5256, 1990.

[3] Keyes, J. W., and Hains, F. D., "Analytical and Experimental Studies of Shock Interference Heating in Hypersonic Flows," NASA TN D-7139, 1973.

[4] Watts, J. D., "Flight Experience with Shock Impingement and Interference Heating on the X-15-2 Research Airplane," NASA TM X-1669, 1968.

[5] Glass, C. E., Holden, M. S., and Wieting, A. R., "Effect of Leading Edge Sweep on Shock-Shock Interference at Mach 8," AIAA paper 89-0271, 1989.

[6] Berry, S. A., Horvath, T. J., DiFulvio, M., Glass, C., and Merski, N. R., "X-34 Experimental Aeroheating at Mach 6 and 10," Journal of Spacecraft and Rockets, Vol. 36, No. 2, 1999, pp. 171-178.

[7] Hiers, R. S., and Loubsky, W. J., "Effects of Shock-Wave Impingement on the Heat Transfer on a Cylindrical Leading Edge," NASA TN D-3859, 1967.

[8] Bushnell, D. M., "Interference Heating on a Swept Cylinder in Region of Intersection with a Wedge at Mach Number 8," NASA TN D-3094, 1965.

[9] Bushnell, D. M., "Effects of Shock Impingement and Other Factors on Leading-Edge Heat Transfer," NASA TN D-4543, 1968.

[10] Berry, S. A., and Nowak, R. J., "Effects of Fin Leading Edge Sweep on Shock-Shock Interaction at Mach 6," AIAA paper 96-0230, 1996.

[11] Singh, D. J., Kumar, A., and Tiwari, S. N., "Three-Dimensional Shock-Shock Interactions on the Scramjet Inlet," AIAA paper 90-0529, 1990.

[12] Bird, G. A., "Three-dimensional Shock-Cylinder Interactions in Hypersonic Flow," AIAA paper 2006-7937, 2006.

[13] Bird, G. A., *Molecular Gas Dynamics and the Direct Simulation of Gas Flows*, Clarendon Press, Oxford, 1994.

[14] Biedron, R. T., et al., "FUN3D Manual: 13.2", NASA TM-2017-219661, 2017.

[15] Burt, J. M., Josyula, E., and Boyd, I. D., "Novel Cartesian Implementation of the Direct Simulation Monte Carlo Method," Journal of Thermophysics and Heat Transfer, Vol. 26, No. 2, 2012, pp. 258-270.

[16] Schwartzentruber, T. E., Scalabrin, L. C., and Boyd, I. D., "Hybrid Particle-Continuum Simulations of Hypersonic Flow over a Hollow-Cylinder-Flare Geometry," AIAA Journal, Vol. 46, No. 8, 2008, pp. 2086-2094.

[17] Lofthouse, A. J., "Nonequilibrium Hypersonic Aerothermodynamics Using the Direct Simulation Monte Carlo and Navier-Stokes Models," PhD. dissertation, University of Michigan, 2008.

[18] Wang, W., and Boyd, I. D., "Predicting Continuum Breakdown in Hypersonic Viscous Flows," Physics of Fluids, Vol. 15, No. 1, 2003, pp. 91-100.

[19] Boyd, I. D., Chen, G., and Candler, G. V., “Predicting Failure of the Continuum Fluid Equations in Transitional Hypersonic Flows,” Physics of Fluids, Vol. 7, No. 1, 1995, pp. 210-219.

[20] Burt, J. M., and Josyula, E., “Continuum Breakdown Effects on Surface Properties for Hypersonic Shock Wave-Boundary Layer Interaction,” AIAA paper 2013-2782, 2013.

[21] Ohlorst, C. W., et al., “Development of X-43A Mach 10 Leading Edges,” 56th International Astronautical Congress, paper IAC-05-D2.5.06, 2005.

[22] Steeves, C. A., He, M. Y., Kasen, S. D., Valdevit, L., Wadley, H. N. G., and Evans, A. G., “Feasibility of Metallic Structural Heat Pipes as Sharp Leading Edges for Hypersonic Vehicles,” Journal of Applied Mechanics, Vol. 76, 2009, 031014.

[23] Bird, G. A., “The Q-K Model for Gas-Phase Chemical Reaction Rates,” Physics of Fluids, Vol. 23, 2011, 106101.

[24] Burt, J. M., and Josyula, E., “Efficient Direct Simulation Monte Carlo Modeling of Very Low Knudsen Number Gas Flows,” AIAA paper 2014-0697, 2014.

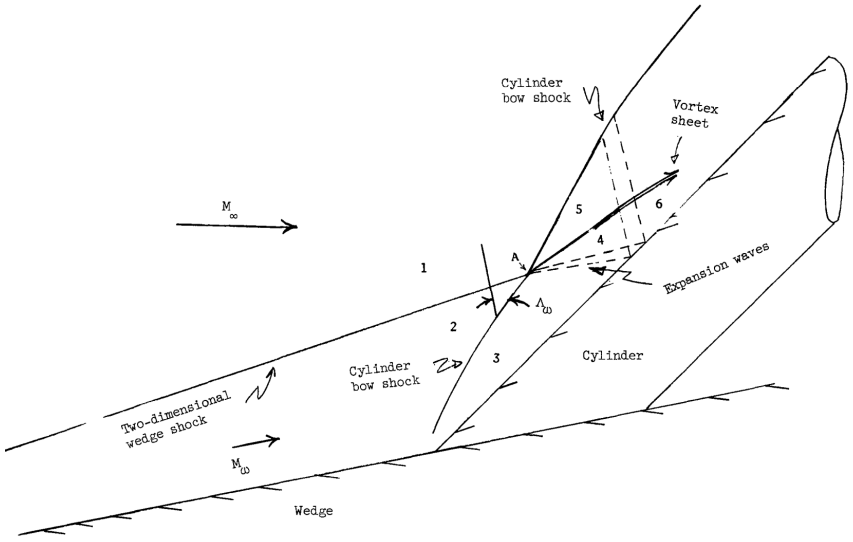

Figure 1. Schematic from Bushnell [8] describing the general flowfield characteristics observed from the cylinder-wedge experiments.

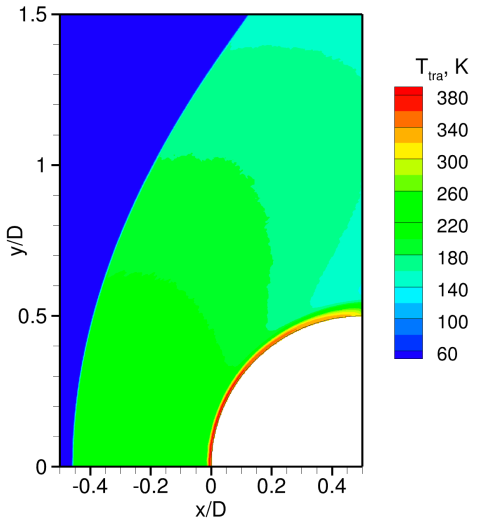

Figure 2. Translational temperature contours for baseline two-dimensional DSMC case.

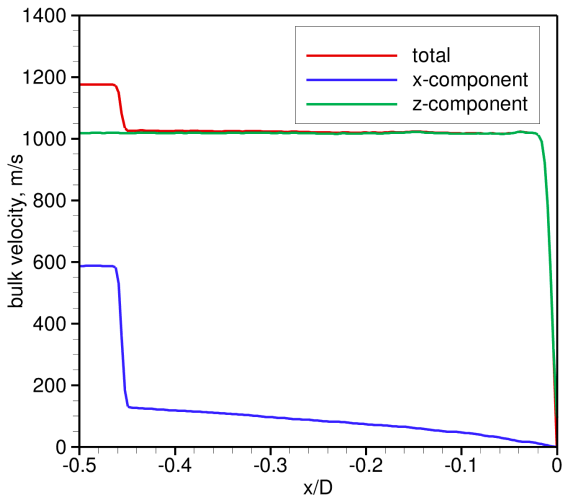

Figure 3. Bulk velocity components along stagnation streamline for baseline two-dimensional DSMC case.

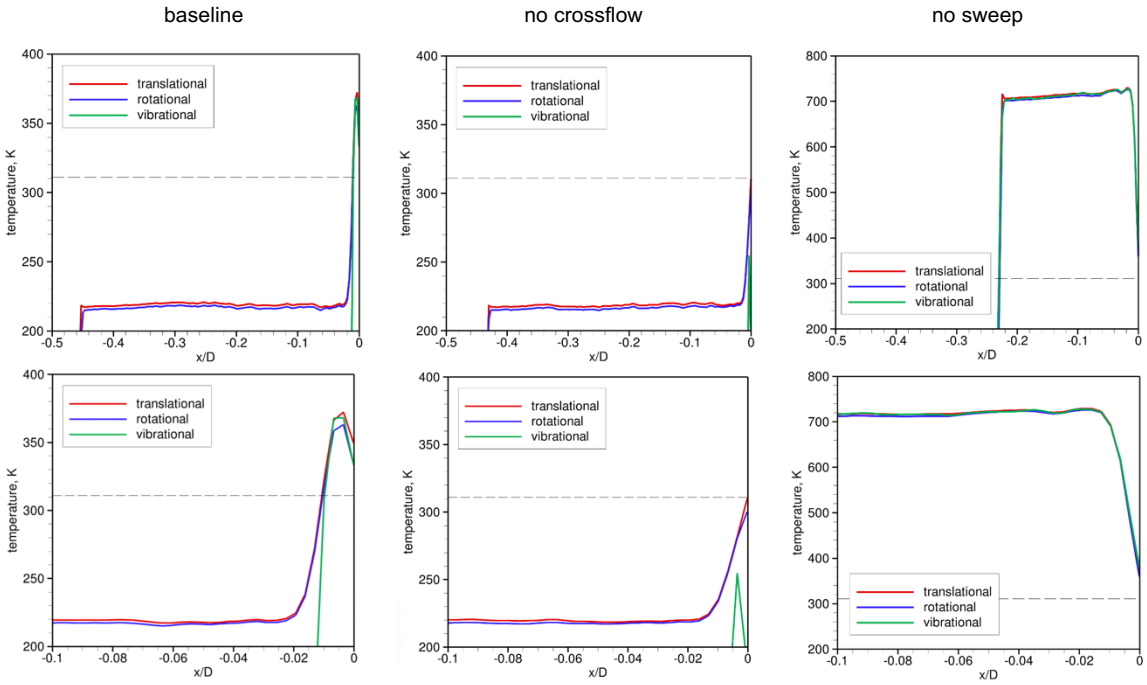

Figure 4. Translational, rotational, and vibrational temperatures along stagnation streamline for baseline (left), “no crossflow” (center), and “no sweep” (right) two-dimensional DSMC cases. Full shock layer temperature profiles are shown on top row, and bottom row displays closeup views around thermal boundary layer and stagnation point. Isothermal wall temperature is indicated by dashed horizontal lines.

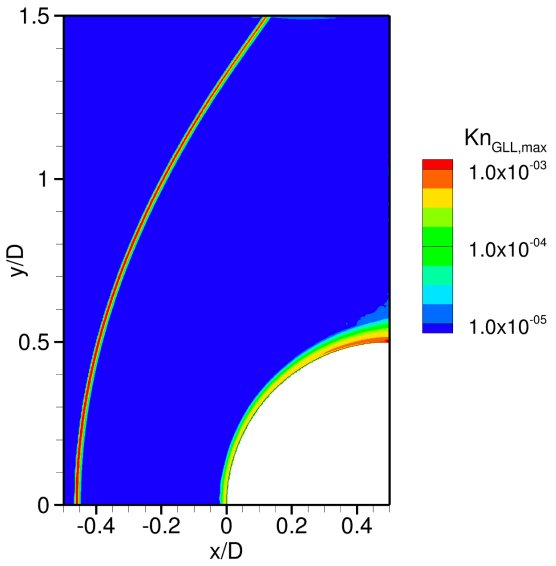

Figure 5. Contours of maximum gradient length local Knudsen number for baseline two-dimensional DSMC case.

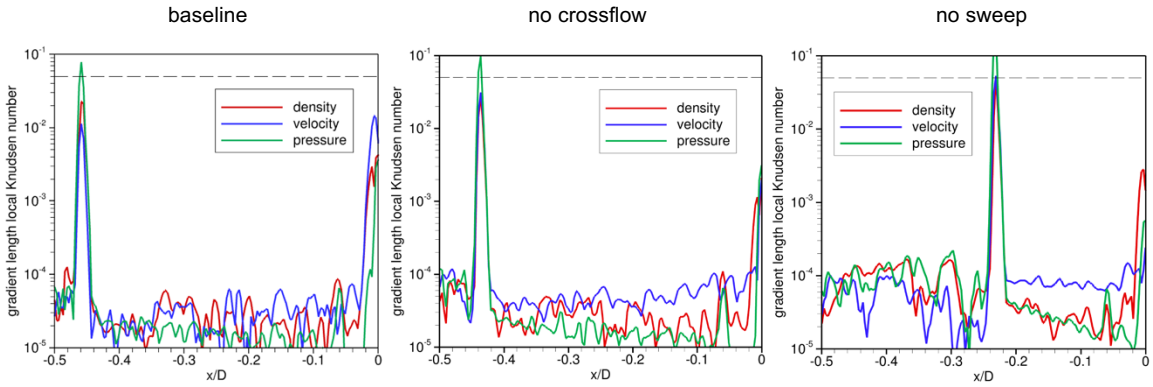

Figure 6. Variation in gradient length local Knudsen numbers along stagnation streamline for two-dimensional DSMC cases. Dashed horizontal lines denote estimated threshold for continuum breakdown.

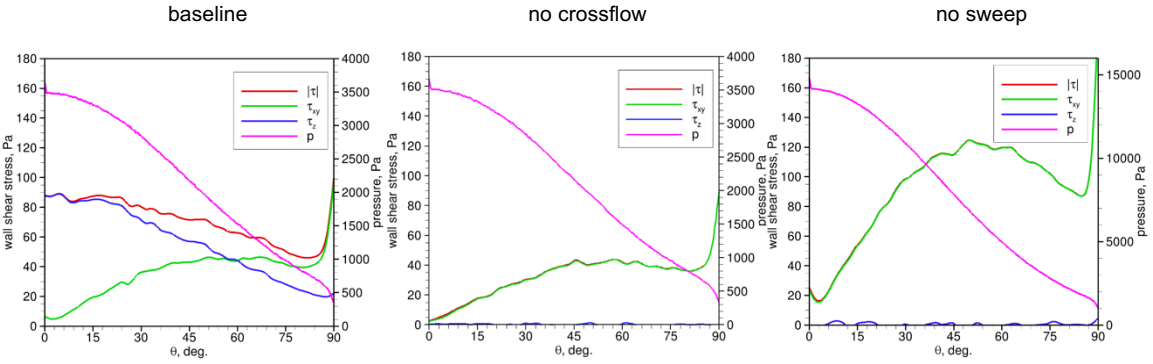

Figure 7. Wall shear stress components and surface pressure plotted as functions of angle θ relative to x- axis.

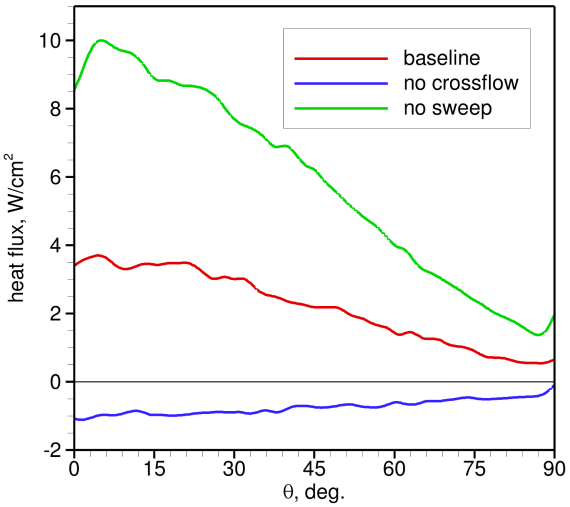

Figure 8. Surface heat flux variation for two-dimensional DSMC cases.

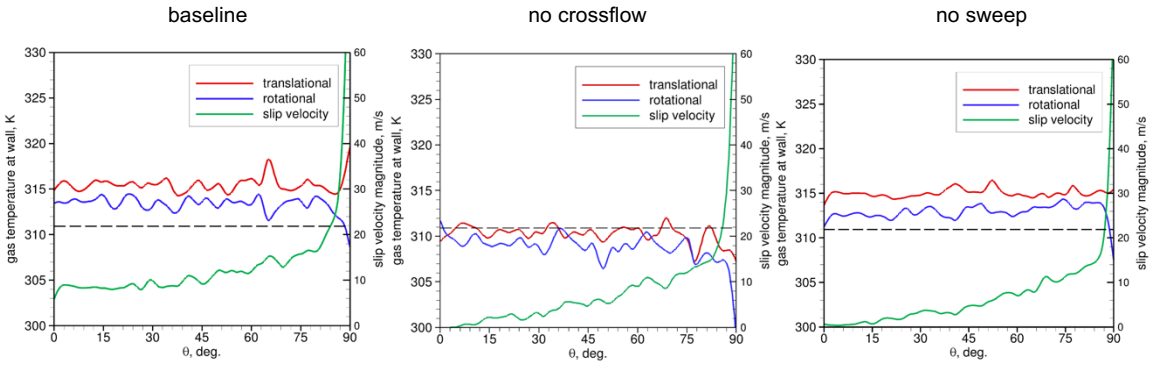

Figure 9. Gas translational and rotational temperatures at wall, and wall slip velocity magnitude, for two-dimensional DSMC cases. Isothermal wall temperature is represented by dashed horizontal lines.

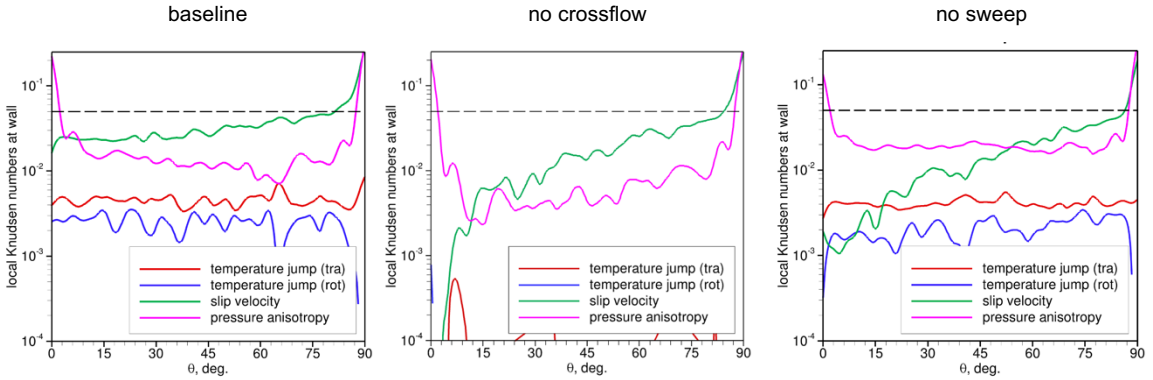

Figure 10. Local Knudsen numbers based on wall quantities for two-dimensional DSMC cases. Dashed horizontal lines denote notional threshold for continuum breakdown.

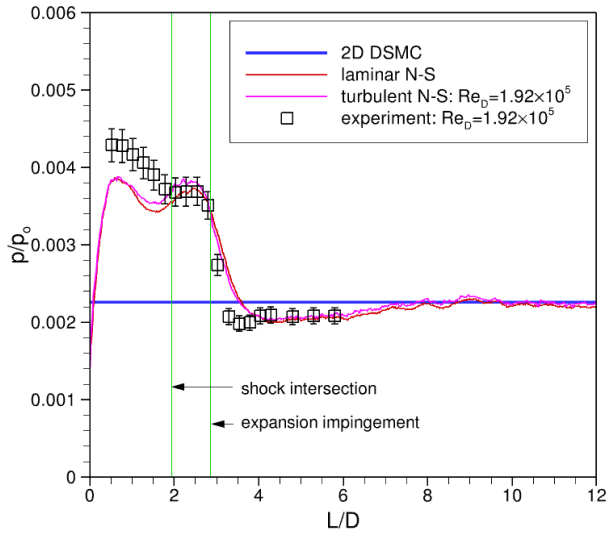

Figure 11. Normalized stagnation line pressure from experiment [8] and from laminar (Re_D = 8.9×10^4) and turbulent (Re_D = 1.92×10^5) N-S simulations. Surface pressure at stagnation point from baseline two-dimensional DSMC simulation is given by blue horizontal line, and green vertical lines indicate locations of experimentally observed flowfield structures.

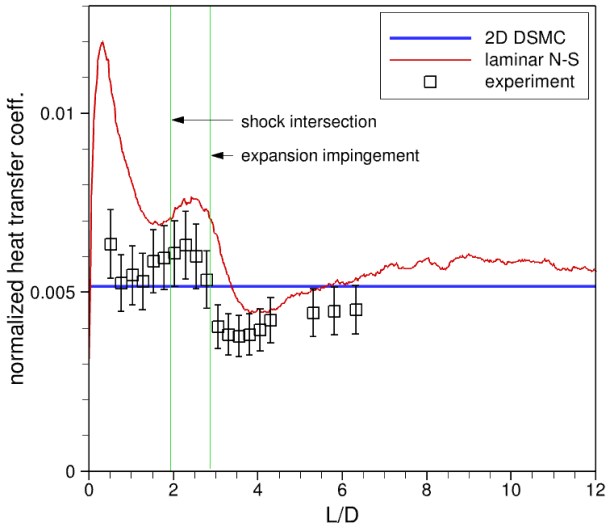

Figure 12. Normalized wall heat transfer coefficient along stagnation line from experiment [8] and laminar N-S simulation. Blue horizontal line represents stagnation point heat transfer coefficient from baseline two-dimensional DSMC simulation.

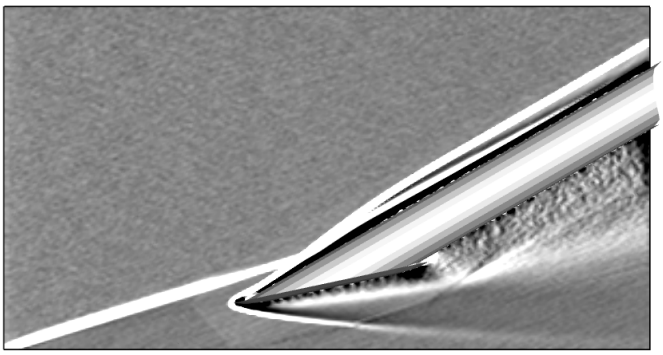

Figure 13. Synthetic Schlieren image based on symmetry plane density gradient from DSMC simulation with T_{wall} = 1200 K at representative flight conditions.

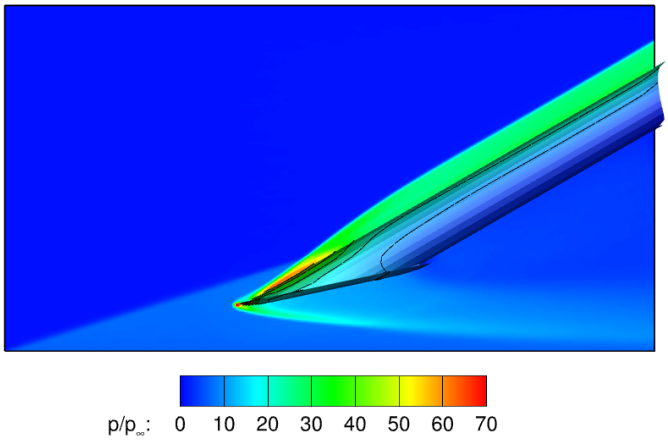

Figure 14. Normalized pressure contours along symmetry plane and cylinder surface at flight conditions.

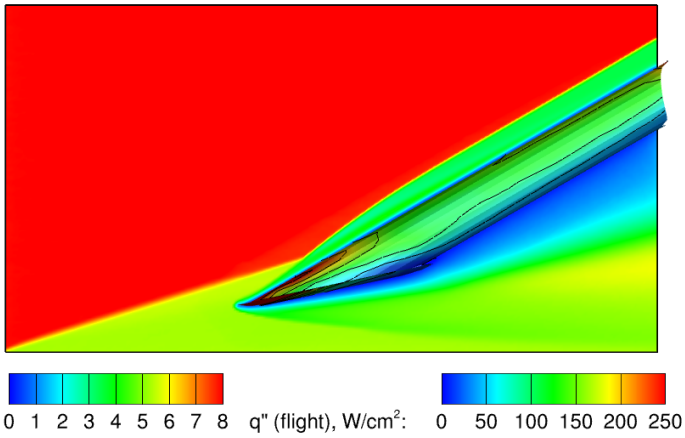

Figure 15. Contours of Mach number along symmetry plane and surface heat flux at flight conditions.

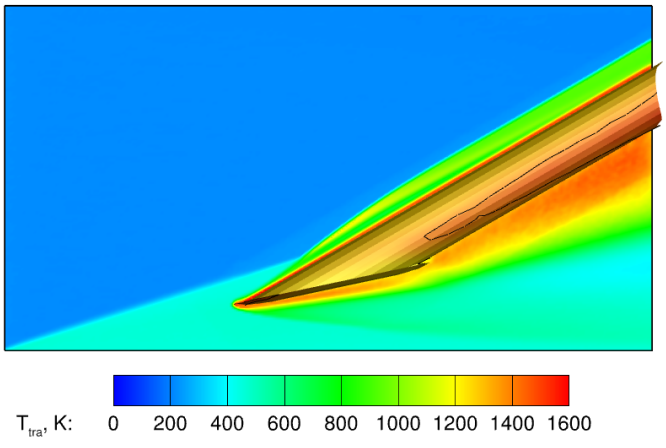

Figure 16. Contours of (a) translational, (b) rotational, and (c) vibrational temperatures along symmetry plane and cylinder surface at flight conditions.

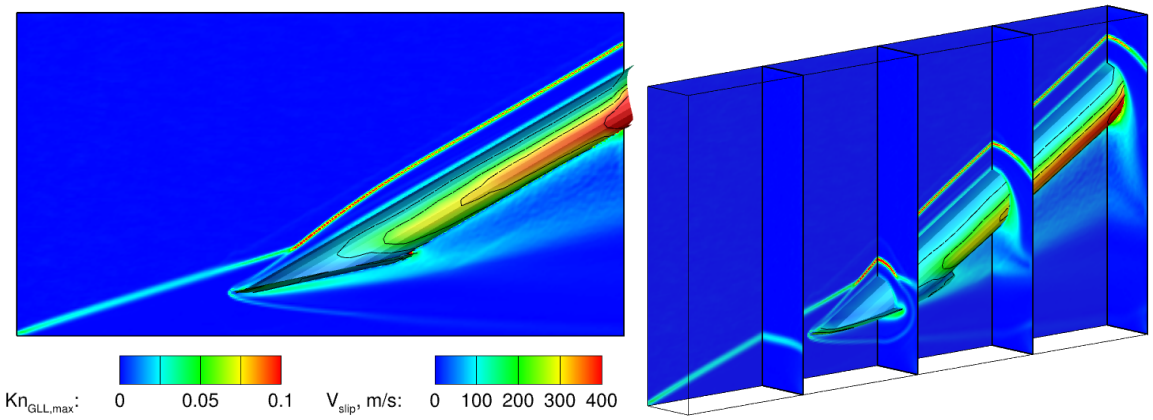

Figure 17. Axis-aligned (left) and isometric (right) views of maximum gradient length local Knudsen number and wall slip velocity magnitude at flight conditions.

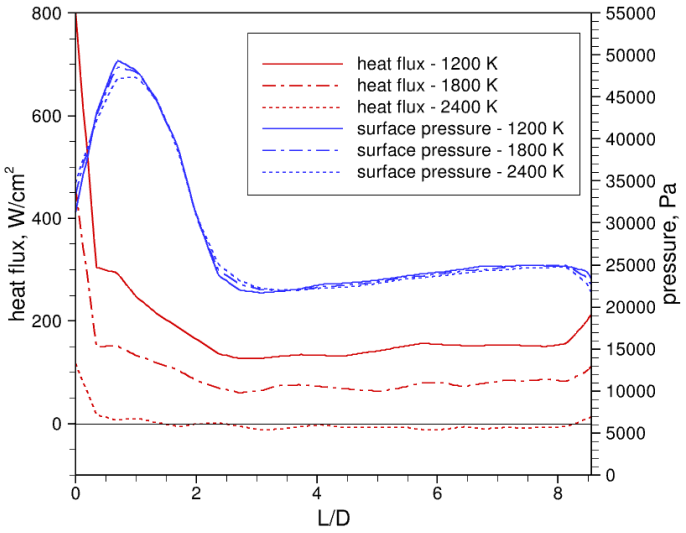

Figure 18. Surface heat flux and pressure along stagnation line from DSMC simulations at flight conditions.

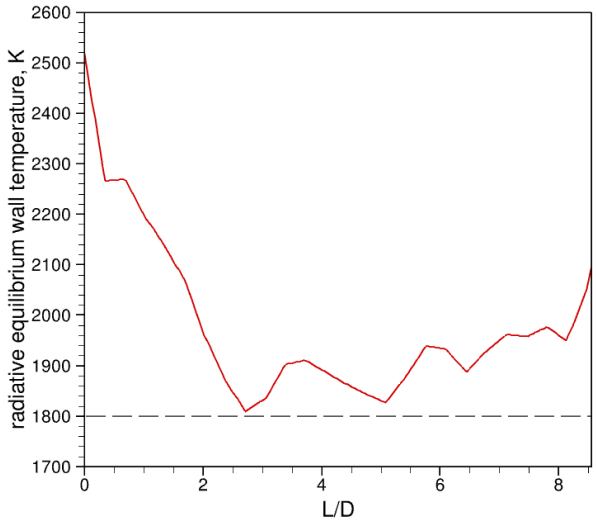

Figure 19. Estimated radiative equilibrium wall temperature along stagnation line at flight conditions. Dashed horizontal line denotes isothermal wall temperature used in DSMC simulation.

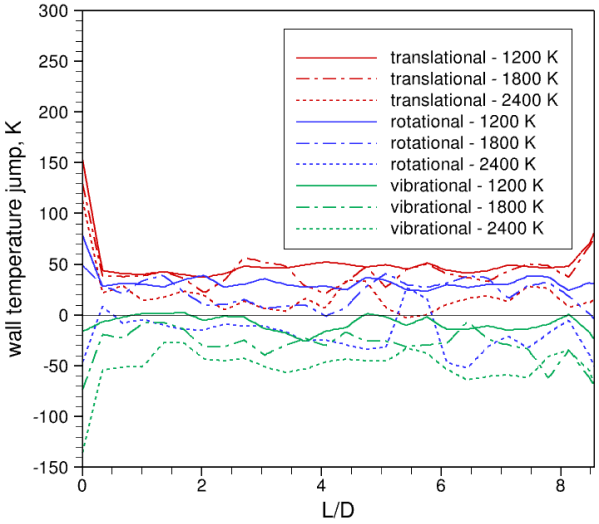

Figure 20. Wall temperature jump along stagnation line for DSMC simulations at flight conditions. Colors indicate energy mode (translational, rotational, or vibrational), and line patterns indicate prescribed wall temperature.

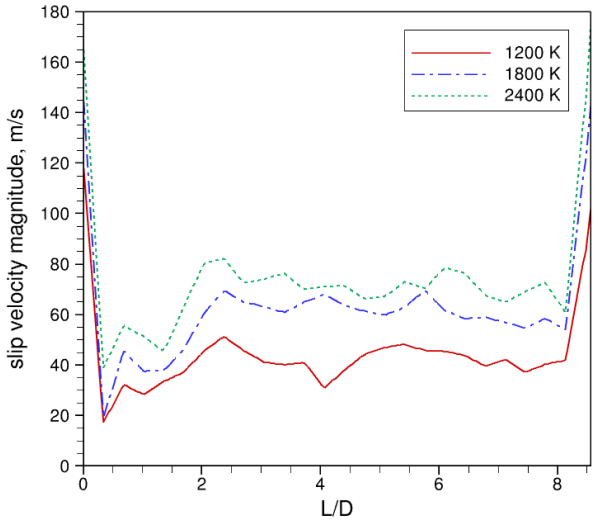

Figure 21. Wall slip velocity magnitude along stagnation line from DSMC simulations at flight conditions.

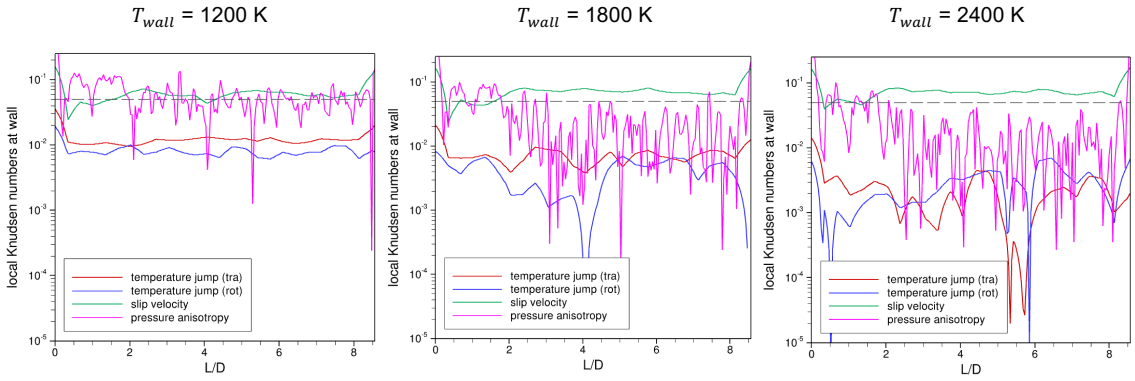

Figure 22. Local Knudsen numbers based on wall quantitites along stagnation line, for various isothermal wall temperatures. Approximate threshold for continuum breakdown is represented by dashed horizontal lines.

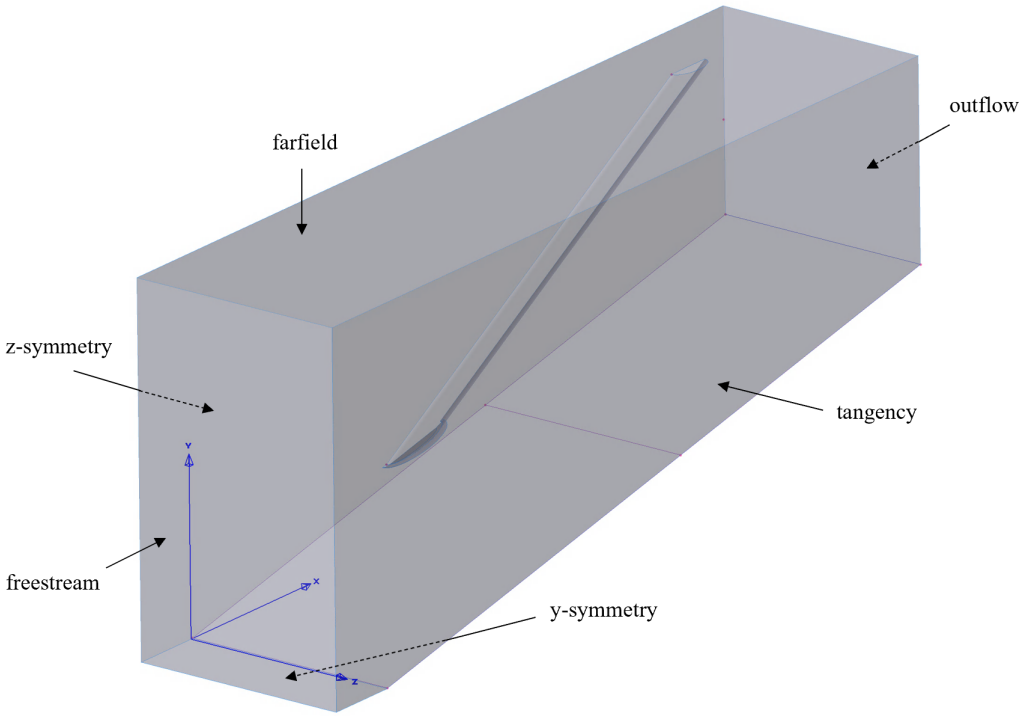

Figure 23. Schematic of wedge-cylinder computational domain.

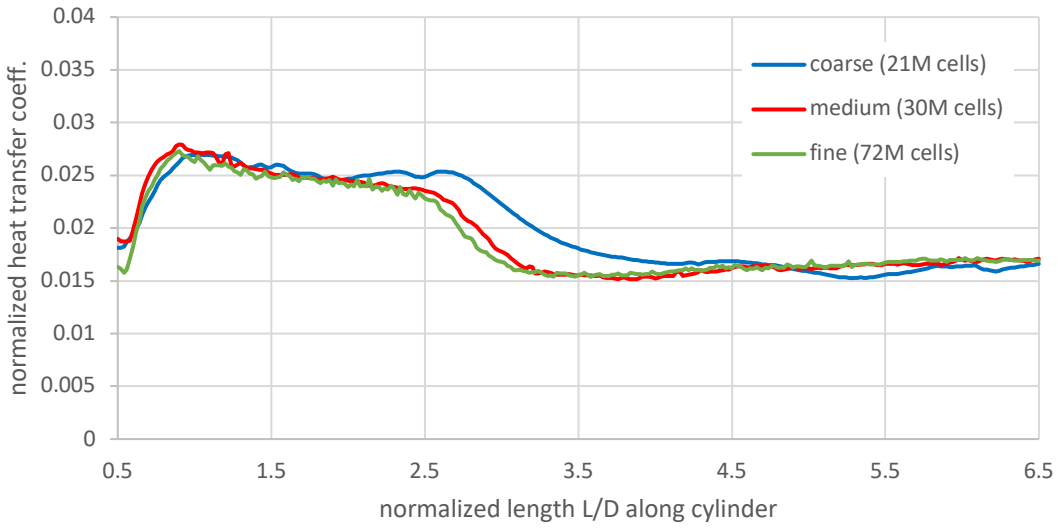

Figure 24. Normalized heat transfer coefficient along the centerline of the cylinder for three levels of mesh refinement.

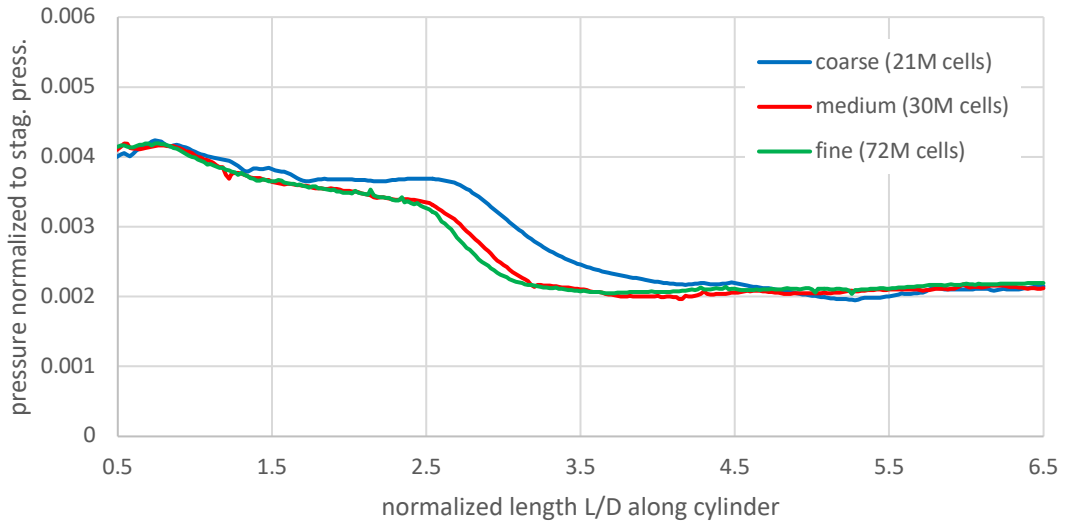

Figure 25. Pressure normalized with respect to the freestream total pressure along the centerline of the cylinder for three levels of mesh refinement.

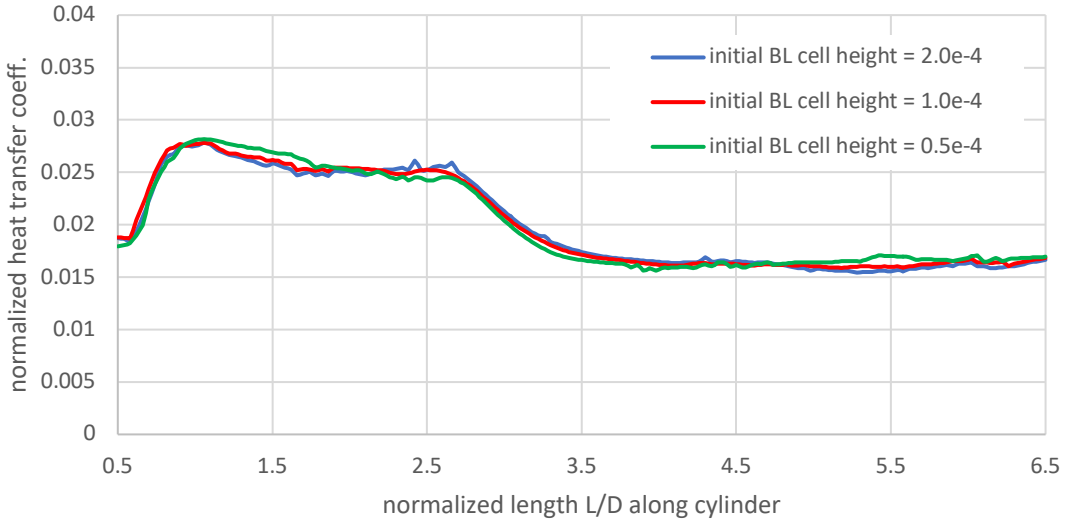

Figure 26. Normalized heat transfer coefficient along the centerline of the cylinder for three initial BL cell heights for the same coarse surface mesh (cell height units are in inches).

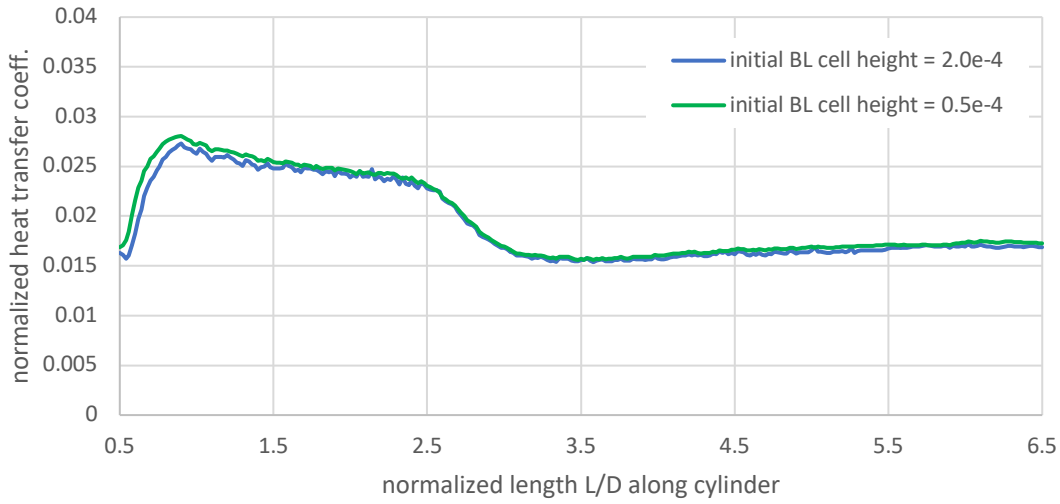

Figure 27. Normalized heat transfer coefficient along the centerline of the cylinder for two initial BL cell heights for the same fine surface mesh (cell height units are in inches).

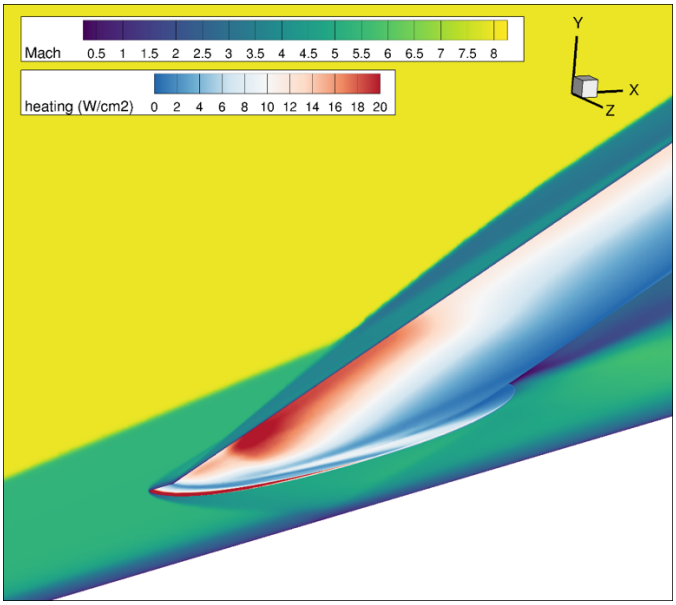

Figure 28. Mach contours and heating contours from the turbulent flow simulation for Re_D = 2.58×10^5.

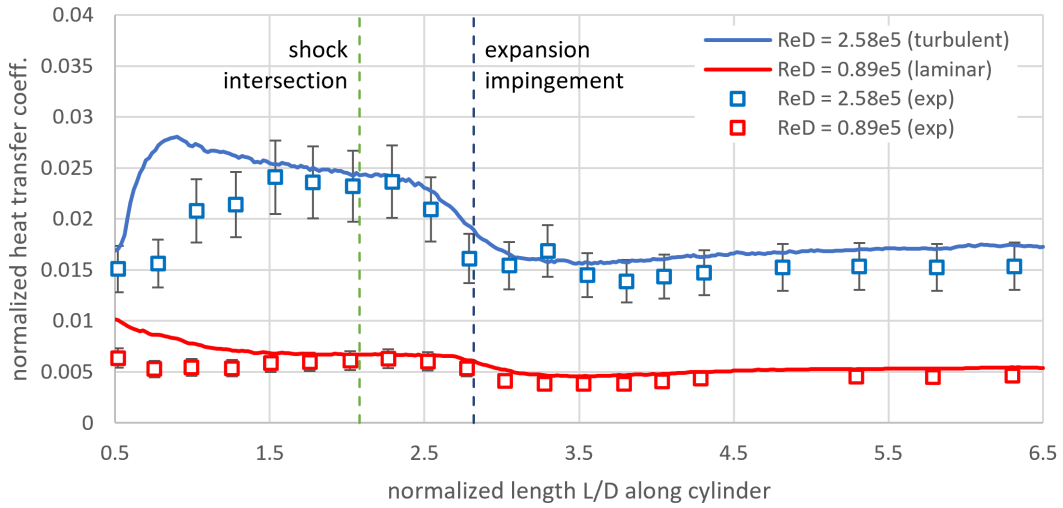

Figure 29. Comparison between normalized heat transfer coefficient from CFD vs. experimental results from Bushnell [8] for turbulent and laminar flow cases.

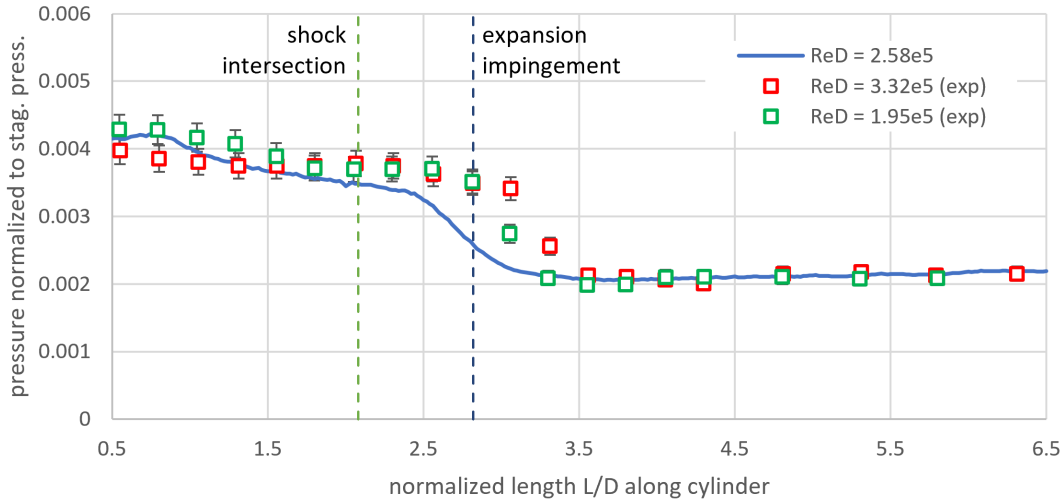

Figure 30. Comparison between pressure normalized with respect to the freestream total pressure from CFD vs. experimental results from Bushnell [8].